batteries

MDPI

Article

Model-Based Performance Evaluation of Hybrid Solid-State Batteries: Impact of Laser-Ablated Geometrical Structures

Maximilian Scheller [1,2,*], Axel Durdel [1], Alexander Frank [1] and Andreas Jossen [1]

[1] Chair of Electrical Energy Storage Technology, Department of Energy and Process Engineering, School of Engineering and Design, Technical University of Munich, Arcisstraße 21, 80333 Munich, Germany
[2] TUMint Energy Research GmbH, Lichtenbergstraße 4, 85748 Garching bei München, Germany
* Correspondence: maximilian.scheller@tum.de

Abstract: Due to challenges in manufacturing composite cathodes with oxide solid electrolytes, new cell concepts are emerging in which the infiltration of solid-polymer electrolyte (SPE) into 3D cathode pore structures improves capacity retention and cycling stability. However, the performance limitation and the resulting practical relevance of such a hybrid concept have not yet been analyzed and discussed. This study investigates the impact of laser-ablated geometric structures on the performance of hybrid solid-state batteries (SSBs). A Doyle–Fuller–Newman modeling approach is developed and parameterized for structured hybrid SSBs that incorporate a PEO/LiTFSI SPE and an LLZO ceramic separator, as well as NMC-811 and Li-metal for the positive- and negative-electrode active materials. Comparison between structured and planar cell designs reveals significant rate capability improvements in structured designs due to reduced diffusion and interfacial charge transfer polarization. A sensitivity analysis of geometric structure parameters shows further potential for performance improvement in terms of specific capacity and energy density. However, current constriction effects in the LLZO separator can deteriorate the rate capability. A more general perspective is then taken by analyzing the impact of changing SPE parameters. An energy density of 128 Wh kg^{-1} at 1C, and 220 Wh kg^{-1} at 1C with improved SPE parameters is achieved in the best case, approaching the target of 250 Wh kg^{-1}, which is currently achieved for conventional Li-ion batteries.

Keywords: hybrid solid state; DFN model; geometric cell design; polymer transport limitation; performance optimization

Citation: Scheller, M.; Durdel, A.; Frank, A.; Jossen, A. Model-Based Performance Evaluation of Hybrid Solid-State Batteries: Impact of Laser-Ablated Geometrical Structures. *Batteries* **2024**, *10*, 392. https://doi.org/10.3390/batteries10110392

Academic Editor: Hirotoshi Yamada

Received: 2 October 2024
Revised: 30 October 2024
Accepted: 31 October 2024
Published: 5 November 2024

1. Introduction

In recent years, lithium-ion batteries (LIBs) have enabled great technological progress in mobile applications and electric vehicles [1]. In strong evolving markets, the cost and performance requirements for next-generation batteries are also becoming more stringent. The SSB is one of the most promising representatives due to advances in the ionic conductivity of inherently safe solid electrolytes (SEs) in combination with high-energy lithium (Li)-metal anodes [2,3]. Different material classes of SEs—namely oxides, halides, sulfides, and polymers—show different advantages and disadvantages in terms of electrochemical stability, ionic transport properties, interface, interphase formation, or mechanical properties, which have already been discussed in several articles [4–7]. Ceramic oxides and especially the garnet-type lithium lanthanum zirconium oxide, $Li_7La_3Zr_2O_{12}$ (LLZO), is unique due to its processability in ambient atmosphere, mechanical strength, and electrochemical stability towards low-anode and high-cathode potentials, as well as intrinsic high-temperature stability [8]. Current state-of-the-art literature shows that Li-metal anode plating and stripping capacities up to 5 mAh cm^{-2} at 2.5 mA cm^{-2} could be reached by using a dense LLZO separator in contact with a 3D porous LLZO layer as an Li-metal host [9]. A similar Li anode concept was used by Shi et al. [10], where Li was infiltrated in a porous 3D LLZO host structure. This stable anode concept was used to further investigate and optimize the rate performance of Li-S cells.

To match the requirements of high-energy densities, thick composite cathodes are needed that are able to provide high-capacity loadings. However, processing such high-energy composite cathodes that deliver sufficiently high performance at the same time is currently the major challenge when using LLZO as an SE since high-temperature co-sintering of active material (AM) and ceramic SEs comes with material degradation and large interface resistances, or large void formation [11,12]. Ihrig et al. [13] proposed filling the remaining voids by additional infiltration with a polymer electrolyte. Their results show that this approach led to minimized interfacial resistances and resulted in a percolated network. Their 100 µm thick LFP-LATP composite cathodes, infiltrated with an MEEP polymer, show a nearly full cathode active material (CAM) utilization and an area-specific storage capacity of more than 3 mAh cm^{-2}. In contrast to ceramic SEs, SPEs help to achieve and maintain a high contact surface to the AM and compensate for AM volume changes due to their flexible and soft nature [14]. Furthermore, electrochemical instabilities of the AM in contact with ceramic SEss could be addressed with SPEs buffer layers [10]. The major disadvantage of SPEss with Li-ion conductive salts is poor ionic transport at room temperature, with conductivities around 10^{-5} S cm^{-1}, diffusivity of 10^{-9} cm^2 s^{-1}, and a low transference number of typically < 0.3. This leads to polarization and performance issues, which are typically mitigated by cycling and characterizing batteries at elevated temperatures between 60 °C and 90 °C [15–17]. Furthermore, the additional interface between the SPE and inorganic solid electrolyte (ISE) affects ionic transport in hybrid cell concepts. Studies using impedance spectroscopy show that charge transfer resistance at this interface strongly depends on the conductive salt content in the SPE, leading to a significant voltage drop [18–20].

Alternative ways of manufacturing ceramic composite cathodes exist to avoid co-sintering with the active material. The common goal is to create a porous ceramic SE host structure with a sintering process, followed by an infiltration process of a slurry mixture containing CAM, an SPE, and additives. The first part of Table 1 lists experimental-based studies regarding composite cathodes using different methods to achieve a 3D porous ceramic electrolyte structure, which are summarized in the following. More detailed information on the presented methods can be found in the listed literature in Table 1. Polymer pore formers are often used as a template to create a defined pore structure. The structure template is filled with LLZO powder and is subsequently sintered to remove the template polymer structure [21]. Another common method is freeze-casting, which generates LLZO green bodies with a directed pore structure, followed by a subsequent sintering process [22–24]. As a third method, laser ablation is used to generate directed 3D structures in a dense ceramic SE pellet. The laser beam passes the ceramic SE in multiple cycles to increase the material removal and handle the structure depth as described in Kriegler et al.'s work [25]. Micrometer-sized structures with varying dimensions and depths can be precisely fabricated. The process is adaptable to other oxide solid electrolytes by adjusting the laser parameters, demonstrating the material versatility of laser ablation [25]. Laser-induced, directed 3D structures were already analyzed in terms of their impact on the performance of liquid electrolytes and lithium-ion batteries. By laser-structuring of graphite anodes, the cell's rate capability and lifetime could be increased due to the reduction in the electrode tortuosity and a reduced risk of lithium plating, respectively [26–28].

Summarized in the second part of Table 1, different simulation-based studies elaborate on achievable energy densities and the performance of 3D-structured composite cathodes. Clausnitzer et al. [29] used a 3D microstructure modeling approach to analyze the impact of vertically aligned channels of inorganic SE LPSCL on the performance of NMC/LPSCL composite cathodes. Since the migration-dominated transport in the porous LPSCL phase did not limit cell performance, a structuring approach to reduce tortuosity in the LPSCL SE phase and enhance Li-ion transport did not result in significant performance gain. An increase of max. 14 Wh kg^{-1} (relative estimates to 8%) could be achieved at roughly 1.1C current load.

Table 1. Overview of studies regarding 3D structuring in SSBs.

Experimental-Based Studies			
Ref.	**Topic**	**Solid Electrolyte Material**	**Structuring Method**
Ji (2022) [30]	3D microchannel high-rate and long-cycling ceramic battery	LLTO	Sintering pore former
Li (2019) [21]	3D garnet structure, polymer infiltration	Ga-LLZO + PEO/LiTFSI	Sintering pore former
Kriegler (2022) [25]	3D-directed structured ceramic with laser ablation	LATP	Laser ablation
Shen (2019) [22]	Oriented 3D-LLZO structures for battery application	LLZO	Freeze-casting
Shen (2020) [23]	Porous 3D-LLZO freeze-tape-casting	LLZO	Freeze-casting
Buannic (2018) [24]	Dense freeze-cast LLZO with open porosity, polymer infiltration	LLZO + Polymer	Freeze-casting
Xu (2021) [31]	3D-micropatterned garnet	LLZO	Laser ablation
Jangid (2023) [32]	Improved rate capability by 3D architectures	Graphite	Mechanical-press with 3D mold
Zekoll (2018) [33]	Hybrid electrolyte 3D-garnet	LLZO	3D-printed template + sintering
Modeling and Simulation-Based Studies			
Ref.	**Topic**	**Solid-Electrolyte Material**	**Model Type**
Kriegler (2024) [34]	Energy content of scaffold-based ASSB	LATP and LLZO	Theor. calculations
Bielefeld (2022) [35]	Cone-type structures filled with AM	LPSCL	3D mircostructure
Wu (2022) [36]	Self-supporting composite cathode and laser drilling	LFP-CM	3D electrolyte transport
Clausnitzer (2024) [29]	Inluence of electrode structuring on ASSB performance	LPSCL	3D microstructure
This work	Impact of structure geometry on hybrid cell performance	SPE + LLZO	p3D

p3D = pseudo-three-dimensional model.

In summary, a suitable processing route to enable ceramic composite cathodes includes an infiltration step of an additional ionic conductive polymer electrolyte. The resulting hybrid cell concept, by using ceramic and polymer SE, enables a stable ionic percolation network in the composite cathode, which can improve composite cathode performance. Different processing routes to achieve a 3D ceramic host structure are described and laser ablation is identified as a scaleable manufacturing route to obtain a directed pore structure.

The hybrid cell concept in this study combines the advantages of the high electrochemical, mechanical and temperature stability of the LLZO SE and avoidance of degradation during co-sintering of AM and LLZO with the concept of using a 3D ceramic host structure and subsequent infiltration of SPE and AM. Compared to other fabrication routes for ceramic host structures, laser ablation allows for a high degree of flexibility in the geometric design of the directed pores, which could then be easily modified in a fabrication line. Disadvantages of the concept may arise due to cost reasons, as SE material is ablated during the laser treatment. Therefore, analysis of the cost of the laser ablation process and the application of laser treatment to non-ceramic SEs may be of interest for future studies.

Taking into account the state-of-the-art simulation studies, a research gap was identified because the interplay between the limited ionic transport in the SPE, the additional interfacial resistance at the SPE | ceramic SE, together with the influence of directed structures, is unknown. To the best of our knowledge, there are no studies that detail the performance of hybrid SSBs with a 3D-structured ceramic composite cathode and an additional infiltrated ion-conducting polymer.

The aim of this work is to analyze the effect of laser-ablated 3D-directed pore structures on the charging performance of a ceramic–polymer hybrid solid-state battery. For comparison, a "classical" planar cell design without a 3D structure using an LLZO separator and a polymer composite cathode is considered. This is achieved by utilizing an adapted physicochemical modeling approach with the additional consideration of material-phase boundaries. Thus, the resulting lithium-ion transport pathways, the limiting transport mechanisms, and the sensitivities with respect to the geometrical design variations could be identified.

The structure of this work is as follows. First, in the modeling section, the physicochemical modeling approach is introduced, and model adaptations due to the use of 2D geometry and additional phase boundaries are explained. Starting with an initial physicochemical parameterization, and a detailed dimensioning of the geometric structure, the different sensitivity studies are introduced and described in detail to achieve maximum

transparency on changing model parameters. Furthermore, the 2D adaptation of the polarization calculation method proposed by Nyman et al. [37] and the procedure for calculating the evaluated energy densities and specific capacities are presented. In the results section, the charge rate capability of the initial structured geometric design is first evaluated and then compared to the equivalent planar cell design. Individual fractions of the total polarizations are presented and the main limiting transport mechanisms are discussed. Subsequently, the results of the geometric sensitivity studies are evaluated and interpreted by taking into account the influence of previously identified limiting mechanisms in the hybrid cell concept. Finally, the practical relevance of the structured hybrid cell concept is discussed in light of general energy and power density targets for SSBs.

2. Modeling

In this work, the physics-based model approach of the Doyle–Fuller–Newman (DFN) model [38,39], often equivalently designated as the pseudo-two-dimensional (p2D) model approach, is used. This approach has already been used for SSBs with binary salt SPEs or single-ion conducting ISEs, in addition to the classic use case of modeling liquid electrolyte cells [40,41]. To capture the internal states of a structured 3D cell geometry, a 1D model domain, as used in the p2D model for a classical planar cell design, is not sufficient. Therefore, at least a 2D geometry is needed. The 2D model domains plus the additional pseudo-dimension is referred to below as the pseudo-three-dimensional (p3D) model and is used to describe the electrochemical behavior of the hybrid solid-state battery cell.

Figure 1a describes the procedure to obtain a structured model cell design based on the concept proposed by Kriegler et al. [25]. Starting with laser ablation of a dense LLZO pellet, a line structure was obtained, which was subsequently infiltrated with the cathode slurry containing the CAM and SPE electrolyte.

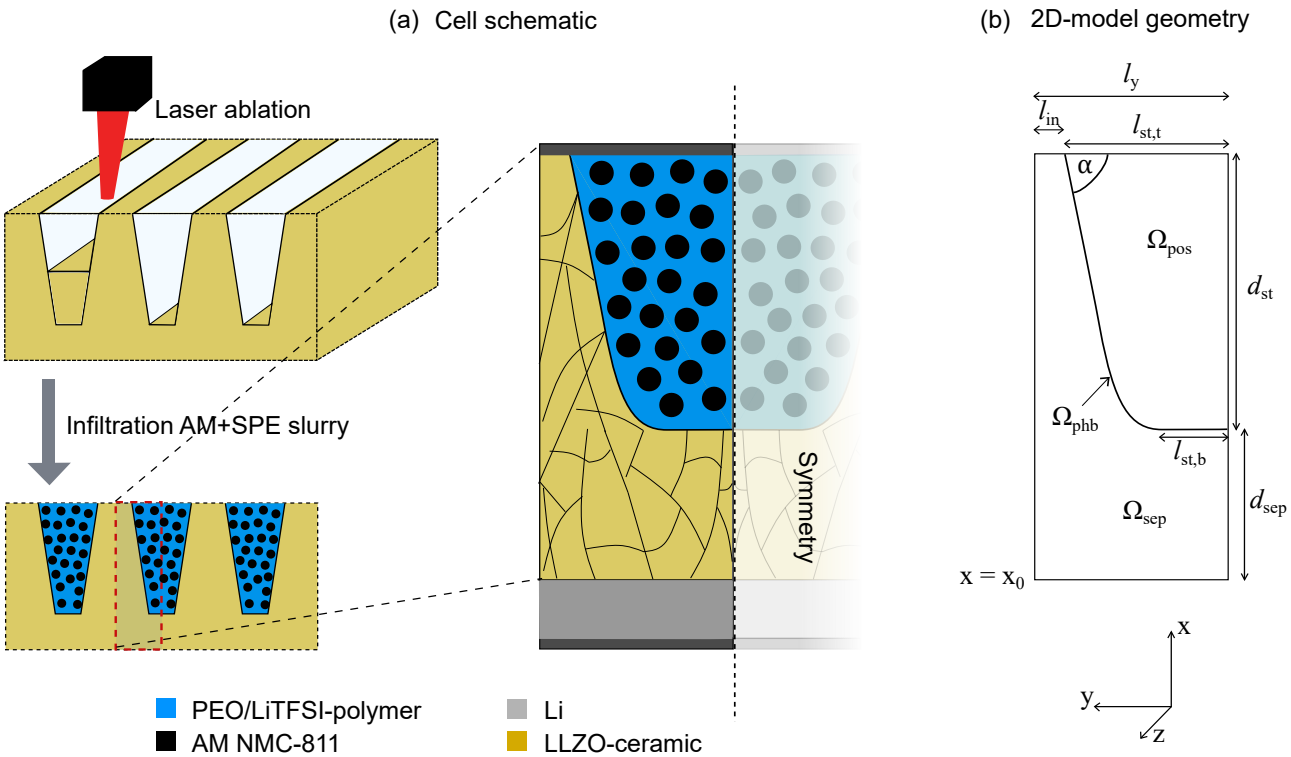

Figure 1. (**a**) Process chart to obtain a structured cell design with laser ablation and subsequent infiltration of cathode slurry containing AM and SPE. Due to symmetry conditions in the z- and y-plane, the geometry can be reduced to 2D. (**b**) The resulting unit cell 2D-model geometry including the dimensioning of geometric parameters and spatially resolved LLZO model domain Ω_{sep} and cathode domain Ω_{pos}.

From a modeling perspective, the real 3D geometry can be simplified into a 2D model geometry without any loss of information due to geometry symmetry in the z- and y-plane. The resulting unit cell model geometry is depicted in Figure 1b and consists of the spatially resolved LLZO domain Ω_{sep} and the composite cathode domain Ω_{pos} in the x- and y-plane as presented in Figure 1b. The Li-metal anode is modeled as a boundary condition at $x = x_0$ to account for charge transfer at the LLZO | Li interface. No spatial resolution of the Li-metal electrode or the aluminum and copper current collector is necessary due to their high electronic conductivity and minor impact on cell performance. Due to immobile anions in the single-ion conducting LLZO SE, Li ions in Ω_{sep} are transported solely migration-based due to gradients in the electric potential. Concentrated solution theory, which captures Li-ion transport by migration and diffusion, was used to account for ionic transport in the SPE phase in Ω_{pos}. To account for additional charge transfer at the SPE | LLZO material phase boundary Ω_{phb}, an additional purely Butler–Volmer (BV)-like reaction kinetics is incorporated as described in our previous publication and adapted here regarding the implementation for the 2D geometry [42]. Therefore, the additional potential drop from the SPE | LLZO charge transfer was calculated via an analytical formulation of the BV equation according to Equation (1), which can be used as a simplification due to a transfer coefficient of $\alpha_{phb} = 0.5$ [43]:

$$\Delta\varphi_{\Omega_{phb}}(x,y,t) = \frac{2\mathcal{R}\,T}{\mathcal{F}}\,arcsinh\left(\frac{i_{\Omega_{phb}}(x,y,t)}{2i_{0,\Omega_{phb}}(x,y,t)}\right) \tag{1}$$

This additional potential drop has to be considered in the governing equations. As a result, the following boundary conditions on Ω_{phb} has to be fulfilled:

$$i_{\Omega_{phb}}(x,y,t) = i_{SPE}(x,y,t) = i_{LLZO}(x,y,t) \tag{2}$$

$$J_{Li,\,SPE}(x,y,t) = J_{Li,\,LLZO}(x,y,t) \tag{3}$$

$$J_{Li,\,SPE}(x,y,t) = -D_{Li,\,SPE}(x,y,t)\,\nabla\,c_{Li,\,SPE}(x,y,t) + \frac{i_{SPE}(x,y,t)\,t_+^{SPE}(x,y,t)}{\mathcal{F}} \tag{4}$$

$$J_{Li,\,LLZO}(x,y,t) = \frac{i_{LLZO}(x,y,t)}{\mathcal{F}} \tag{5}$$

$$\Delta\varphi_{\Omega_{phb}}(x,y,t) = \varphi_{LLZO}(x,y,t) - \varphi_{SPE}(x,y,t) \tag{6}$$

In order to better interpret the results of the simulation study, the model assumptions are presented below.

Material degradation and related side reactions due to temperature-dependent or electrochemical material instabilities are neglected in the model. To ensure an electrochemically stable model system, the upper cut-off cell voltage in this study is set to 4 V instead of around 4.3 V for nickel-rich AM to avoid electrochemical instability between the PEO/LiTFSI SPE and the nickel-rich AM as observed in the literature [44,45]. In addition, an ideal contact between the AM and SPE as well as between the SPE and LLZO is assumed. This is based on the results of Wetjen et al. [44], who analyzed the microstructure of PEO/LiTFSI-based composite cathodes. Their SEM images showed fully embedded and homogeneously distributed NCA-CAM particles in the SPE matrix, resulting in good mechanical contact between the SPE and CAM. To achieve sufficient non-limiting electronic conductivity in the composite cathode, inactive additives such as carbon binder are considered in the electrode morphology by assuming an inactive volume of $\varepsilon_{add} = 3$ vol %.

For modeling and simulations, the entire system is assumed to be isothermal at $T = 80$ °C at all times. The model equations are depicted in Table A1 and are solved using COMSOL Multiphysics® 6.1. The solver settings are unchanged from the default ones recommended by the software for the given set of equations.

2.1. Parameterization

The parameters used for the simulations with respect to the microstructure, the material transport, the kinetics and the cell are listed in Table A2. The composition of the composite cathode is chosen based on the study by Kriegler et al. [25] to obtain a functional cell design. Therefore, the cathode consists of $\omega_{AM} = 88\,wt\,\%$ NMC-811, $\omega_{SPE} = 10\,wt\,\%$ SPE, and $\omega_{add} = 2\,wt\,\%$ conductive additive, resulting in volumetric proportions of $\varepsilon_{AM} = 66\,vol\,\%$, $\varepsilon_{SPE} = 31\,vol\,\%$, and $\varepsilon_{add} = 3\,vol\,\%$, respectively [25]. According to the literature, functional cells are produced with an SPE volumetric fraction in the range of 20 vol % to 43 vol % [12,13]. To achieve complete penetration of the slurry into the laser-ablated structure during infiltration, the particle size must be chosen to match the bottom structure size $l_{st,b}$. Therefore, the particle radius of the CAM was chosen to be $R_p = 1\,\mu m$. Proper infiltration is expected with the chosen particle size since the smallest bottom part of the structure in this study is $l_{st,b} = 7.5\,\mu m$. The ionic tortuosity factor in the SPE phase is set to $\tau = 4$ [46].

The Li-ion transport parameters in the SPE phase in the composite cathode domain Ω_{pos} are defined depending on the Li-ion concentration in the SPE phase, as measured in the study of Pesko et al. [15]. The initial salt concentration was chosen to be $c_{Li,SPE} = 1960\,mol\,m^{-3}$. The resulting initial polymer parameter values are listed in Table A2.

The work of Pesko et al. [15] showed that modeling species transport in PEO/LiTFSI-based polymer electrolytes by concentrated solution theory led to a high agreement of simulation and experimental results for the electrolyte potential. This is why concentrated solution theory, together with their set of concentration-dependent polymer parameters, is used in this study. In the recent literature, the theory of species transport in polymer electrolytes is extended by the effect of solvent motion [47]. Mistry et al. [47] showed that polymer motion due to frictional coupling between ions and charge-neutral species could affect Li-ion transport and resulting concentration gradients. Their results indicate a non-negligible impact of solvent motion on Li-ion velocity and the resulting concentration gradient at a higher salt concentration, as tested with $c_{Li,SPE} = 2580\,mol\,m^{-3}$. Their work is fundamental, but up to now, has been limited to symmetric Li-polymer-Li cell concepts with a thick 500 µm layer of polymer electrolyte. As discussed in the latest work of Mistry et al. [48], future work on measuring and analyzing the effect of solvent motion on the pore-scale level in intercalation electrodes is needed.

The interface exchange current density between LLZO | PEO at Ω_{phb} is also defined depending on the salt concentration $c_{Li,SPE}$, since the charge transfer resistance at the material phase boundary decreases with increasing salt concentration [18,49,50]. This is of particular relevance since the total cell performance of a hybrid SSB containing ceramic/polymer SE phase boundaries shows a high sensitivity to changes in the interface kinetics, as discussed in our previous study [42].

The equilibrium potential of the Li-metal anode is set to 0 V. The quasi open-circuit potential (qOCP) of an NMC-811 CAM half-cell, measured at 25 °C during delithiation at C/100, was taken from the literature [51]. The entropic heat coefficient of the NMC-811 CAM is small with a maximum value of $\frac{\partial U_{eq}}{\partial T} = -0.075\,mV\,K^{-1}$ at a stoichiometry of $\chi = 0.99$ [51]. The resulting OCP offset at 80 °C is negligible, with a maximum deviation of 4.1 mV, and is therefore neglected in this study.

2.2. Geometric Structure Sensitivity Study

The main part of the simulation study analyzes the effect of laser-ablated structure geometry on hybrid SSB cell performance. For all of the geometric variations presented in the following, the physicochemical parameterization introduced in the previous section remains unchanged. In order to ensure transparency with respect to the varied geometric parameters, a dimensioning of the 2D structured geometry is introduced, as shown in Figure 1b.

A reference geometric design (#1 BASE) of the laser-ablated structures is derived from the experimental study of Kriegler et al. [25] who analyzed their laser-ablated structures with scanning electron microscopy and laser scanning microscopy. From these practically realizable structure designs, the following geometric parameters are extracted.

A structure depth d_{st} between 70 µm and 115 µm was achieved with multiple laser scan cycles for an inorganic oxide LATP SE [25]. The adjacent structures are separated by a residual amount of inactive separator material, which can be characterized by the definition of the inactive width l_{in}. According to Kriegler et al. [25], the laser process was adjusted so that the distance between two adjacent structures was between 10 µm and 35 µm. In the presented unit cell model geometry in Figure 1b, this distance must be interpreted as twice the width l_{in} due to the applied symmetry condition. The top width of the kerf (twice the width $l_{st,t}$) was varied between 45 µm and 80 µm. The #1 BASE was designed conservatively with a structure depth of $d_{st} = 65$ µm, $l_{in} = 10$ µm, and a kerf top width of $l_{st,t} = 20$ µm, as listed in Table 2.

Table 2. Overview of all simulated geometric variations and the associated change in single geometric parameters. Starting with a #1 BASE geometric parameterization derived from Kriegler et al. [25], the analysis of a higher-capacity (#2 HC) version with a deeper structure follows. Based on the #2 HC geometry, the variation in the inactive width l_{in} (study #3) and the structure angle α (studies #4 to #8) follows. The normalized capacity Ω_{pos} of the cathode defines the change in absolute cathode capacity compared to the #1 BASE geometric design.

Study #	Study Name	Geometric Parameters						
		Normalized Capacity Ω_{pos}	l_{in} µm	$l_{st,t}$ µm	$l_{st,b}$ µm	d_{st} µm	α °	d_{sep} µm
#1	BASE	1	10	20	7.5	65	83	20
#2	High Capacity (HC)	1.4	10	22.6	7.5	85	83	20
#3	HC inactive	1.4	{1, 4, 7, 10}	22.6	7.5	85	83	20
#4	HC angle 1	1.4	1	34.9	7.5	63	70	20
#5	HC angle 2	1.4	1	30.6	7.5	69.3	75	20
#6	HC angle 3	1.4	1	25.7	7.5	78.1	80	20
#7	HC angle 4	1.4	1	20	7.5	92	85	20
#8	HC angle 5	1.4	{1, 4}	12	7.5	123	90	20

The thickness of the LLZO separator remains unchanged for all simulations with $d_{sep} = 20$ µm, as does the lower structure width $l_{st,b} = 7.5$ µm. Table 2 lists in detail the different simulated geometries and the associated change in each geometric parameter. An additional visualization of the geometric variations performed is presented in Figure 2.

For the sensitivity study, the structure depth d_{st} was first increased to 85 µm, resulting in a high-capacity (HC) structure design (#2 HC). Compared to the #1 BASE design, the cathode volume and capacity increased by 40%, which results in a normalized capacity Ω_{pos} of 1.4. The HC design serves as the base geometry for the subsequent geometric sensitivity studies. To ensure comparability, the condition of equal cathode volume and capacity must be fulfilled. Secondly, with this, a variation in the distance between the structures, represented by l_{in}, was analyzed for $l_{in} = 10$ µm to 1 µm in the #3 HC inactive study. Thirdly, the structural angle α was varied in subsequent studies #4 through #8. The angle α describes the constriction towards the bottom of the laser-ablated conical structure. In practice, there will be an upper limit for α below 90°, depending on the laser source used for ablation in combination with the material of the workpiece. By setting $\alpha = 90°$ in the sensitivity study #8, the cell behavior at the theoretical limit of the laser-ablated structure geometry can be evaluated.

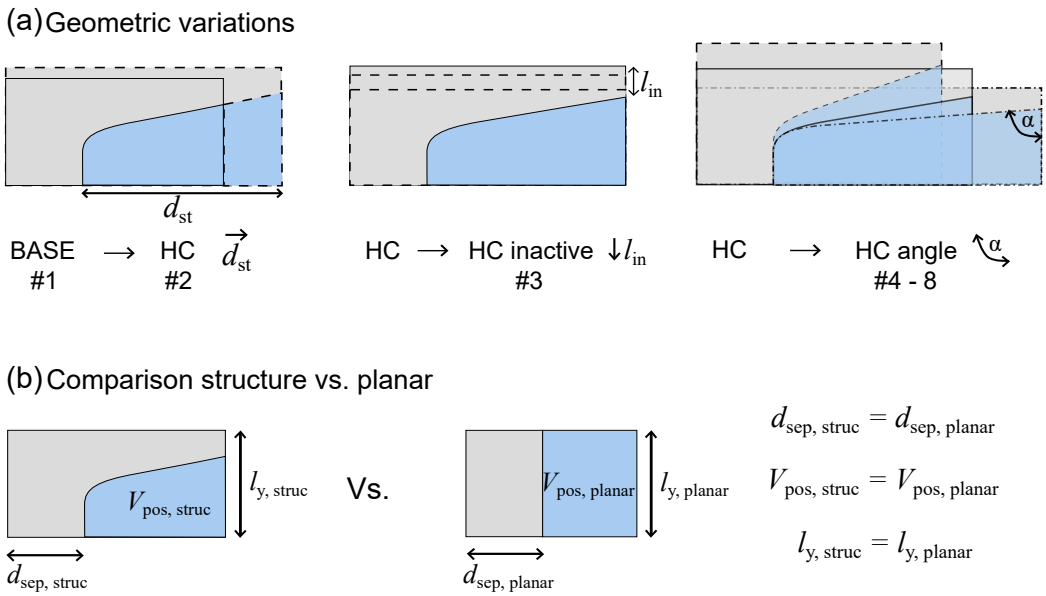

Figure 2. (**a**) Visualization of the geometric variations for analyzing the sensitivity on cell performance. Detailed geometric parameter values for each simulated geometry are listed in Table 2. (**b**) The derivation of the equivalent planar cell design based on the given structured cell design.

For a better interpretation of the cell performance obtained with a structured cell design, equivalent planar cell designs were also derived and simulated, as shown in the lower part of Figure 2. To ensure comparability, the planar geometries are equally designed for the separator thickness d_{sep}, the unit cell width l_y, and the cathode volume V_{pos}, which ensures equal volumetric $Q_{vol,pr}$ and absolute capacity Q_{abs} of the cells as calculated according to Equations (8) and (9).

Based on the capacity, the absolute current to be applied at l_y for the simulations was calculated according to Equation (10). Therefore, an unambiguous definition of the applied current I_{app} was obtained, which ensures comparability between the different simulated cell designs at different c-rates.

$$Q_{vol,th} = Q_{sp,AM}\, \omega_{AM}\, \rho_{pos} \tag{7}$$

$$Q_{vol,pr} = Q_{vol,th}\, (\chi_0 - \chi_1) \tag{8}$$

$$Q_{abs} = Q_{vol,pr}\, V_{pos} \tag{9}$$

$$I_{app,1C} = Q_{abs}\, \mathrm{h}^{-1} \tag{10}$$

The symbols are defined as the specific capacity of the AM $Q_{sp,AM}$, the mass share of the AM ω_{AM}, the density of the electrode ρ_{pos}, and the utilized stoichiometric delta $\chi_0 - \chi_1$.

2.3. Energy and Polarization Calculation

For the comparison between different structured hybrid SSB cell designs and corresponding planar cell designs, three major evaluation parameters are defined in this section. A detailed list of assumed material parameters and calculations to obtain specific capacity and energy densities is presented in Table A4. The main definitions are introduced in the following.

First, the chargeable specific capacity $Q_{sp,ch}$ in mAh g^{-1}, normalized to the mass of the cathode m_{pos}, is used as a global measure for the utilization of the AM during charging, and defined as follows:

$$Q_{ch} = \int_{t_0}^{t_{EoC}} I_{app}\, dt \tag{11}$$

$$Q_{sp,ch} = \frac{Q_{ch}}{m_{pos}} \tag{12}$$

The chargeable capacity Q_{ch} is the charged capacity at the end-of-charge (EoC), as the cell voltage reaches 4 V.

Due to the boundary conditions of identical morphology inside the cathode domain, and identical cathode volume throughout the geometric sensitivity studies #2–#8, the relation between the theoretical cathode capacity and cathode mass remains constant. Therefore, the impact of the structure geometry on the electrochemical performance with increasing c-rate can be clearly identified.

Second, the gravimetric energy density $E_{gr,ch}$ in Wh kg^{-1} is defined according to Equation (14) as the charged energy until the EoC, normalized to the mass of the cell stack m_{stack}. The stack mass is defined as the sum of the mass of current collectors, separator, and cathode as listed in Table A4.

$$E_{ch} = \int_{t_0}^{t_{EoC}} U_{eq} \cdot I_{app}\, dt \tag{13}$$

$$E_{gr,ch} = \frac{E_{ch}}{m_{stack}} \tag{14}$$

In addition to the specific capacity $Q_{ch,sp}$, the energy density $E_{gr,ch}$ captures the impact of inactive mass on cell performance, which changes by varying the structure geometry in the conducted sensitivity studies.

Lastly, the overpotential during charging is introduced as a third evaluation parameter. Following the method by Nyman et al. [37], the total polarization is separated into contributions based on their physicochemical origins and spatial domains. This allows for the resolution of diffusion and ohmic processes in the SPE, ohmic polarization in the single-ion conducting LLZO separator, diffusion-related polarization in the AM, and charge transfer polarization associated with delithiation processes. Additionally, in line with our previous study [42], charge transfer overpotentials at the SPE | LLZO interfaces are also considered. For this study, the calculation method has been extended from 1D to 2D, with the relevant equations presented in Table A5.

3. Results and Discussion

3.1. Impact of Structured Cell Design on Electrochemical Performance—Comparison Base Structure vs. Planar Cell Design

The first part of the Results section deals with a deeper analysis of the impact of the structured cell design on the electrochemical cell performance. In a top–down approach, the rate capability between a structured cell and a "classical" planar design is first compared for the defined evaluation parameters, the specific capacity $Q_{sp,ch}$, and the gravimetric energy density $E_{gr,ch}$, as shown in Figure 3. To gain a deeper understanding of the performance-limiting mechanisms in the different cell designs, the evaluation of single polarization contributions is later presented in Figures 4a and A1. Finally, additional transient and 2D resolution of concentration gradients in the SPE phase and the resulting ionic current distribution are presented in Figure 4b–d.

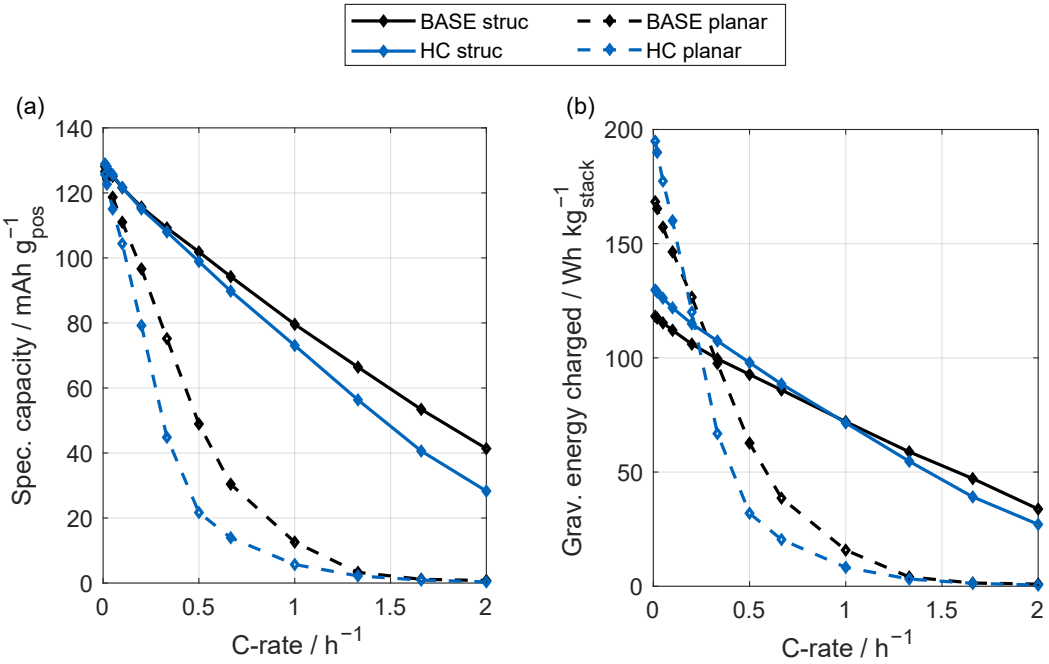

Figure 3. Rate capability of structured cell design and planar equivalent for the #1 BASE (black) and the #2 HC (blue) design. The c-rate is varied from C/100 to 2C, where each marker point represents the respective simulation result, and linear interpolation between the data points visualizes the trend of the rate dependence. Comparison of the chargeable specific capacity $Q_{sp,ch}$ in (**a**), and the resulting gravimetric energy density $E_{gr,ch}$ in (**b**).

As shown in Figure 3a, the rate capability of the structured #1 BASE and #2 HC cell designs is significantly better than their planar counterparts. At a low charging rate of C/100, all cells achieved nearly the maximum specific cathode capacity of 128.1 mAh g^{-1}, indicating identical gravimetric and volumetric capacity, based on the mass and volume of the cathode domain Ω_{pos}. As the c-rate increases, the chargeable specific capacity $Q_{sp,ch}$ decreases for all cells, with a more rapid decline in the planar designs. At 0.5C, the planar BASE design reached only about 50 mAh g^{-1}, while the structured BASE design achieved around 100 mAh g^{-1}.

The gravimetric energy density $E_{gr,ch}$, as shown in Figure 3b, decreases from 168.4 Wh kg^{-1} for the BASE planar design to 118.2 Wh kg^{-1} for the BASE structured design at C/100, which is a 42.5% reduction. This is due to the additional LLZO SE remaining after laser ablation, which increases the volume of the structured cell by 37.7% and its mass by 44.4% due to the high density of LLZO of 5.07 g cm^{-3}. With increasing c-rate, the strong deterioration of the specific capacity observed for the planar cell designs starts to dominate the rate capability behavior of the energy density. For the #1 BASE design, a crossover occurs around C/3, from which, the energy density of the structured design is higher compared to the planar counterpart.

To better understand the performance improvement due to structuring, polarization analysis results are shown in Figure 4a. Comparing the polarization at EoC for planar and structured BASE cell designs, the total polarization is lower in the structured cell across all simulated c-rates. This correlates with the higher specific capacities $Q_{sp,ch}$ observed for the structured cell in Figure 3a, as lower polarization results in better CAM utilization. The most sensitive polarization contributions related to cell design are also identified.

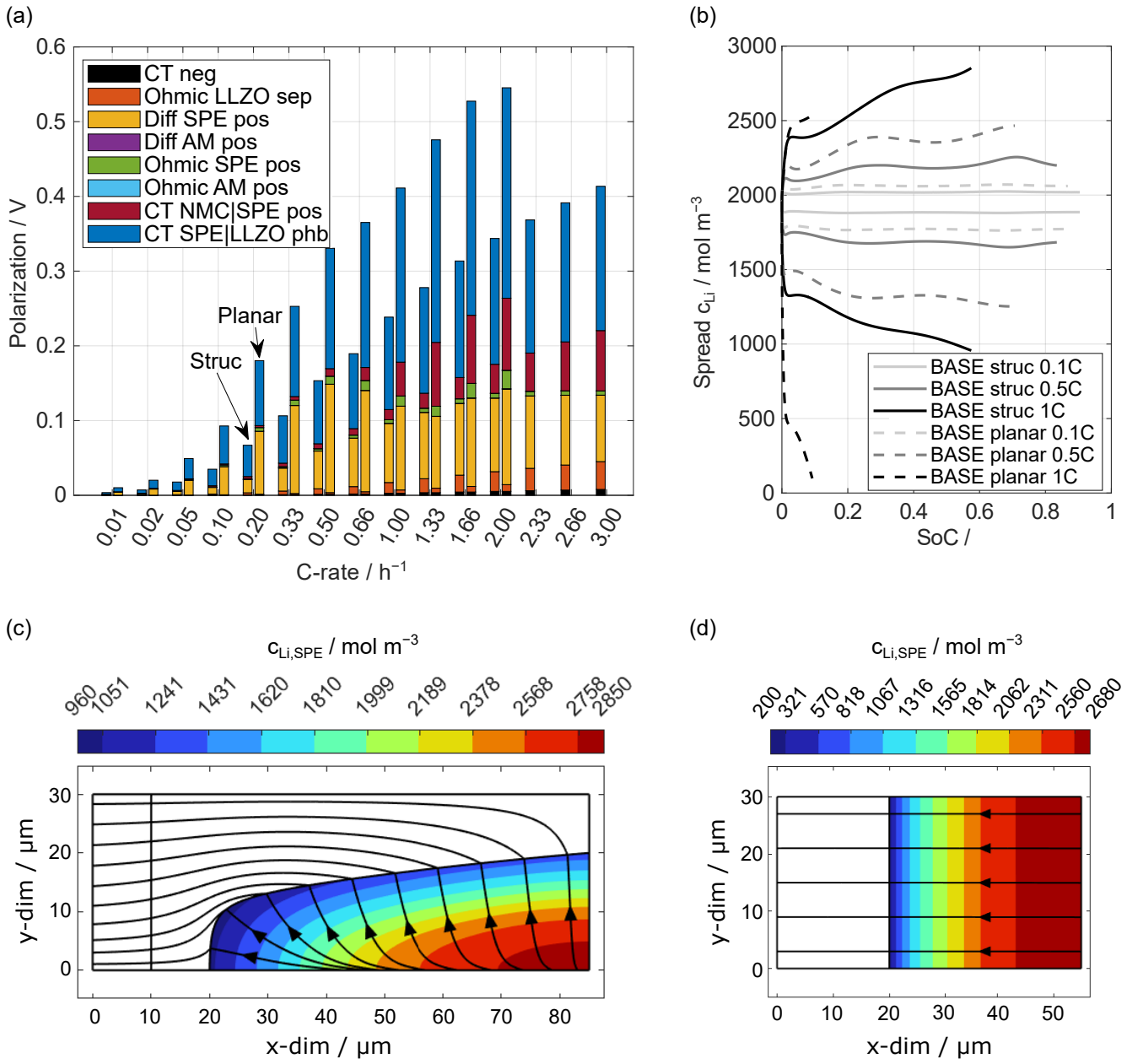

Figure 4. In-depth analysis of performance differences between the #1 BASE structured and planar design. (**a**) End-of-charge (EoC) polarization at $U_{cell} = 4\,\mathrm{V}$ at different c-rates. The shares of polarization due to their physical and spatial origin, as calculated in Table A5, are stacked on top of each other. Therefore, the top end of each bar corresponds to the total polarization for the given rate. (**b**) Comparison of concentration gradients in the SPE phase between BASE structured (solid) and planar (dashed) cell design for a 0.1C, 0.5C, and 1C rate. For each c-rate, the transient development of the maximum and minimum concentrations is depicted, visualizing the spread in $c_{\mathrm{Li,SPE}}$ in domain Ω_{pos}. The equilibrium concentration in the SPE phase is $c_{\mathrm{Li,SPE}} = 1960\,\mathrm{mol\,m^{-3}}$. (**c**,**d**) A 2D visualization of concentration gradients of $c_{\mathrm{Li,SPE}}$ at an EoC of a 1C charge. Streamlines indicate the direction of the Li-ion flux in the SPE phase in the cathode and the LLZO separator phase. Since the concentration in the LLZO phase is constant, only the concentration profile in the SPE phase in the cathode is colored.

Diffusion-based Li-ion transport in the SPE phase within the cathode domain Ω_{pos} (yellow) shows significant improvement in the structured cell design compared to the planar design. At a C/3 charge, the SPE diffusion polarization at EoC decreases from 118 mV in the planar case to 31 mV in the structured scenario. The structured design shortens the Li-ion transport pathways in the cathode domain Ω_{pos}, reducing diffusion length. This is highlighted with the streamlines shown in Figure 4c,d, which illustrate the direction of the ionic current in the SPE phase, propagating in the normal direction to areas of equal concentration. Electrophoretic transport in the SPE (Figure 4a, green color) has minimal impact, as the transference number for PEO/LiTFSI SPE is low, ranging from 0.06 to 0.26, depending on lithium concentration [15].

As the c-rate increases, the difference in SPE diffusion polarization (yellow) between the structured and planar designs decreases, since the planar case does not show significant further increases from 0.5C onward. This is due to evolving Li-ion concentration gradients. Figure 4b shows the evolution of the maximum and minimum Li-ion concentrations in the SPE in Ω_{pos} during charging with C/10, C/2, and 1C for the structured and planar BASE #1 design. With increasing rates, the concentration spread in the SPE phase of the cathode increases for both designs, with the planar design consistently showing higher minimum and maximum concentrations. At a C/2 charge rate, the gradient in the planar scenario continuously increases slightly from the start to the EoC point. This behavior is indicative of diffusion-limited ionic transport. By further increasing the c-rate, the concentration gradients do not fully develop until the EoC criterion is reached, leading to a decrease in the SPE diffusion polarization compared to the structured scenario, as observed in the bar graph in Figure 4a.

The second dominant polarization contribution stems from charge transfer at the material interface Ω_{phb} between LLZO and SPE, which follows BV-like behavior in dependence on the interface current density $i_{\Omega_{phb}}$, according to Equation (1). Due to structuring, the boundary length $l_{\Omega_{phb}}$ increases by a factor of 2.48. This reduces the mean boundary current density for the structured design compared to the planar design. At lower c-rates, the scaling effect is solely due to geometric design changes. At higher rates, concentration inhomogeneities in the SPE phase of Ω_{pos} cause Li-ion depletion near the boundary Ω_{phb}. Figure 4c,d show Li-ion concentration at EoC for 1C charging in both scenarios. The planar design shows stronger depletion at the boundary Ω_{phb} close to EoC, causing the exchange current density $i_{0,\Omega_{phb}}$ to decrease, since the underlying charge transfer resistance $R_{ct,\Omega_{phb}}$ (see Table A2, [15]) increases with decreasing concentration. As a result, a stronger transient increase in charge transfer polarization is observed, as shown in Figure A1. Consequently, the 4 V EoC criterion is reached earlier, impairing charge rate capability.

In summary, the modeling results presented indicate that structuring can be expected to improve the performance of hybrid cell designs consisting of a ceramic LLZO separator and a composite cathode with an ionic conductive SPE. The rate capability was significantly improved for the structured design compared to the planar cell design due to the reduction in the large polarization contributions from SPE diffusion and charge transfer at the LLZO | SPE interface. In terms of energy density, structuring leads to higher material fractions of LLZO, which increases cell volume and weight compared to the planar design. Therefore, a trade-off between improving the specific capacity $Q_{sp,ch}$ and increasing the weight and volume determines the energy density $E_{gr,ch}$. This highlights the importance of further analyzing the sensitivity of the structure geometry with the goal of minimizing additional inactive LLZO SE amounts by maintaining or improving AM utilization.

3.2. Sensitivity Analysis of Geometrical Parameter Variation

To analyze the impact of geometrical parameter variations on cell performance, the sensitivity study listed in Table 2 is evaluated in the following.

Initially, the design of the #1 BASE was modified by increasing the structure depth d_{st} from 65 µm to 85 µm. This enhancement in the laser-ablated structure depth resulted in a 40% increase in absolute cell capacity.

The rate capability performance of the #2 HC design is illustrated in Figure 3. In comparison to the BASE design, the specific capacity $Q_{sp,ch}$ of planar and structured design exhibits stronger fading as the rate increases. This could be expected, as the deeper structure extends the ionic transport pathways, resulting in increased polarization and an earlier EoC at 4 V.

In contrast, the achievable gravimetric energy density $E_{gr,ch}$ of the HC design increases at low c-rates compared to the BASE design, as presented in Figure 3b. This can be explained by the lower relative weight contribution from the current collectors, Li-metal anode, and the separator in relation to the total mass of the cell stack. Therefore, at C/100 charging, the $E_{gr,ch}$ increases by 10% from 118 Wh kg^{-1} in the BASE scenario to 130 Wh kg^{-1} for the HC design. Analogous to the #1 BASE design, the energy density of the HC is dominated by the rate-dependent behavior of the specific capacity, as depicted in Figure 3b. For the HC design, the crossover point between planar and structured design is shifted to a lower rate of C/5 compared to C/3 for the BASE design. This means that the structured design outperforms the equivalent planar design already at a rate of C/5. This indicates that by increasing the cathode capacity, structuring has a higher positive impact on the energy density rate capability.

3.2.1. Variation in the Inactive Width l_{in}

The practical realization of structuring a ceramic SE by laser ablation has limitations regarding the optimization of the structure design. The first practical limitation comes from the separation between adjacent line structures, which is described by the inactive width l_{in}. A minimum limit for l_{in} will appear in the practical laser ablation process to maintain the mechanical stability of the scaffolds and to address the challenges of positioning the laser beam or the workpiece during multiple scan cycles. Therefore, the simulation-based determination of the sensitivity of l_{in} on the cell performance is useful to identify needs or potentials for cell design optimization.

For the sensitivity analysis, different cell designs are analyzed by varying l_{in} from 10 µm to 1 µm in study #3 of HC inactive, as listed in Table 2. All other geometric parameters remain unchanged from study #2 HC. By decreasing l_{in}, the volume and mass of the LLZO separator domain Ω_{sep} decrease, as well as the total volume and mass of the cell, by maintaining the cathode capacity. Therefore, an increase in energy density is expected.

Figure 5b illustrates the rate capability in relation to gravimetric energy density. As expected, at C/100, $E_{gr,ch}$ increases from 130 Wh kg^{-1} for $l_{in} = 10$ µm to 187 Wh kg^{-1} for $l_{in} = 1$ µm, marking a 44% rise. However, with increasing c-rate, the relative gain in $E_{gr,ch}$ diminishes, as indicated by the varying slopes of the curves. In addition to expectations, the energy density is influenced not only by changes in mass but also by polarization variations across different designs, although the geometric and morphological cathode design of Ω_{pos} has not been changed. This is further evidenced by the specific capacity shown in Figure 5a. At higher rates, the cell design with $l_{in} = 1$ µm exhibits lower charge capacities compared to other designs, demonstrating a clear trend of decreasing specific capacity with reduced inactive width as the c-rate increases. Polarization analysis further revealed that the reduction in specific capacity is attributed to increased polarization caused by ionic transport in the LLZO solid electrolyte within domain Ω_{sep}. As l_{in} decreases, the current density in the narrower region of the LLZO SE increases, resulting in increased local polarization. This current constriction in the narrow region can significantly deteriorate cell performance. When decreasing l_{in} from 10 µm to 1 µm, the specific capacity $Q_{sp,ch}$ at 1C decreases from 73.1 mAh g^{-1} to 66.9 mAh g^{-1}, showing a relative decline of 8.5%.

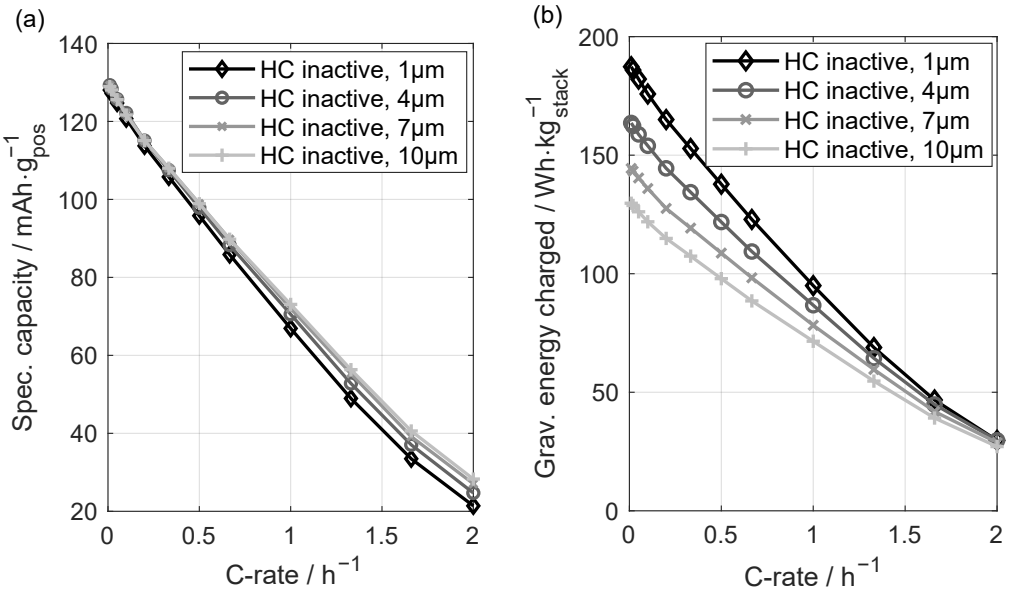

Figure 5. Comparison of the rate capability under variation in the inactive width l_{in} (study #3 of HC inactive; see Table 2). Starting from the HC cell design with $l_{in} = 10\,\mu m$, the inactive width was reduced to $l_{in} = 1\,\mu m$. Results for the specific capacity $Q_{sp,ch}$ in (**a**) and for the gravimetric energy density $E_{gr,ch}$ in (**b**) of the structured designs are presented.

3.2.2. Variation in the Structure Angle α

The second practical limitation of the laser structuring of ceramic SE is the structure angle α. Depending on the laser source used, the process parameters and the material to be ablated, the angle of the characteristic conical structure can vary, as shown in the study by Kriegler et al. [25]. The following section analyzes the sensitivity of the angle α on the cell performance. Therefore, sensitivity studies #4-8 have been defined according to Table 2. As visualized in Figure 2, a change in the structure angle α leads to a change in several other geometric parameters in order to maintain the same cathode capacity compared to the previously conducted sensitivity studies. Detailed values for all geometric parameters are given in Table 2. Since the previous study #3 of HC inactive shows that the energy density could be improved by reducing the inactive width, l_{in} is kept constant during the variation in the angle by fixing it to $l_{in} = 1\,\mu m$.

In Figure 6a, the rate dependency of $Q_{sp,ch}$ is evaluated with varying structure angle α. First, an increase in rate capability can be observed by increasing the angle from 70° to 85°. At 1C, the specific capacity $Q_{sp,ch}$ increases from 51.4 mAh g^{-1} to 67.0 mAh g^{-1}, which is a relative increase of 30%. This trend is reversed when the angle is increased to 90°. As a result, a strong decrease in $Q_{sp,ch}$ can be observed with increasing rates.

To identify the origin of the observed dependence on α, the polarization was analyzed according to Table A5. Each bar in Figure 7 shows the calculated individual proportions of the polarization for the given angle α. First, the total polarization decreases as the structure angle increases from $\alpha = 70°$ to $\alpha = 85°$, which fit the observation of higher specific capacities for increasing α, as shown in Figure 6a. This reduction in total polarization is primarily due to the decreased diffusion polarization within the SPE phase (yellow) in the Ω_{pos} domain, as increasing α reduces concentration gradients. Second, the polarization within the LLZO domain (orange) Ω_{sep} increases with increasing α due to the stronger current constriction in the narrower LLZO region, resulting in higher current densities and local polarization. The electrolyte current density for a structure angle of $\alpha = 85°$ (study #7) and $\alpha = 90°$ (study #8) are presented in Figure A2.

Thus, there is a trade-off between reducing the diffusion polarization in the SPE and increasing the ohmic polarization in the LLZO. In particular, at $\alpha = 90°$, the ohmic polar-

ization in the LLZO phase increases significantly, leading to higher total polarization and reduced charging performance in terms of specific capacity $Q_{sp,ch}$, as shown in Figure 6a.

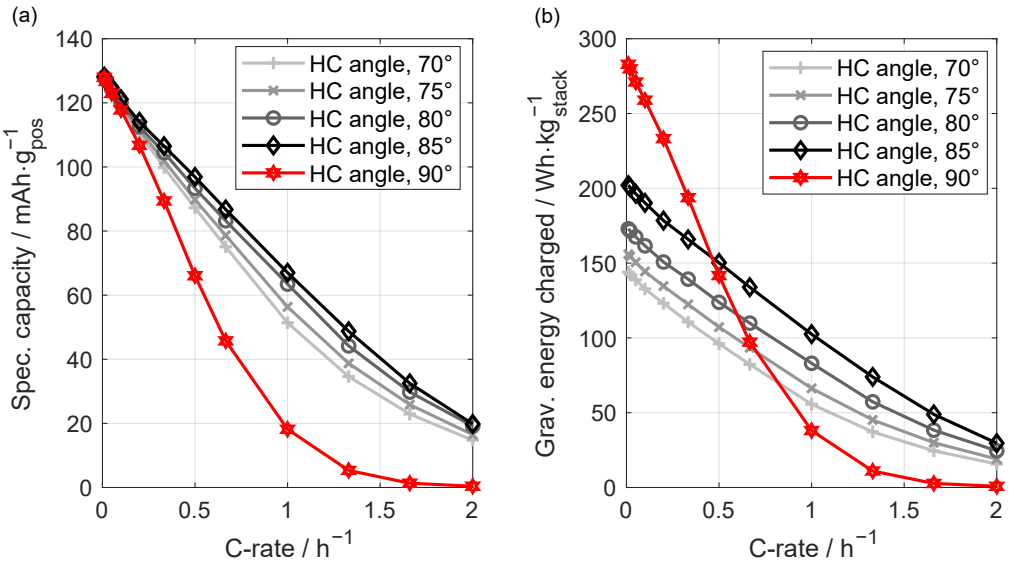

Figure 6. Comparison of the rate capability by evaluation of the specific capacity $Q_{sp,ch}$ in (**a**) and the gravimetric energy density $E_{gr,ch}$ in (**b**) under variation in the structure angle α (studies #4–8 HC angle; see Table 2). The angle α is varied between 70° and 90°, while keeping the inactive width constant with $l_{in} = 1\,\mu m$.

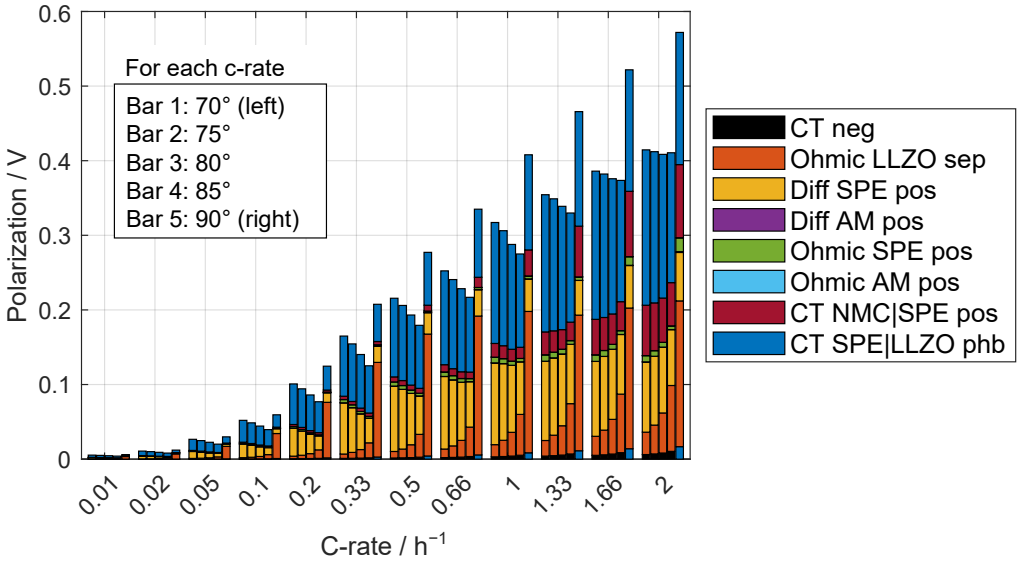

Figure 7. Bar plot presenting the total polarization at EoC for different c-rates. For each c-rate, the five bars present the total polarization for different angles from 70° (far left) to 90° (far right). The different colors represent the shares of polarization due to the spatial and physical origin.

The two main trends observed for the specific capacity are also visible when evaluating the gravimetric energy density $E_{gr,ch}$, according to Equation (14), and become additionally overlayed by varying stack mass due to structure angle variation. Increasing α reduces both the volume and mass of the LLZO domain Ω_{sep}, resulting in a 32% decrease in total cell stack mass as α increases from 70° to 85°. As a result, $E_{gr,ch}$ increases significantly due to the reduction in stack mass along with the improved rate capability of the specific capacity. As shown in Figure 6b, for $\alpha = 85°$, an energy density of 200 Wh kg^{-1} at C/100 and about 100 Wh kg^{-1} at 1C is achieved, representing the best trade-off between energy density and

rate capability of the herein tested geometries. Likewise, the $\alpha = 90°$ design achieves the highest energy density of 283 Wh kg^{-1} at C/100, but exhibits significant deterioration at higher rates due to current constriction.

For completeness, a brief analysis of the current constriction effect is presented. Study #8 examines this by increasing the inactive width, l_{in}, from 1 µm to 4 µm. The red lines in Figure 8 show the results for the energy density rate capability of study #8. The increase in l_{in} to 4 µm improves rate capability by reducing current constriction, but decreases the maximum achievable energy density due to the added mass of the LLZO. Further comparison with previous results in Figure 8 depicts that the cell design with $\alpha = 90°$ and $l_{in} = 4$ µm performs similarly to the structured design in study #7. The effect of current constriction on rate performance is significant and should be considered when optimizing cell structures for specific material combinations and cathode morphologies.

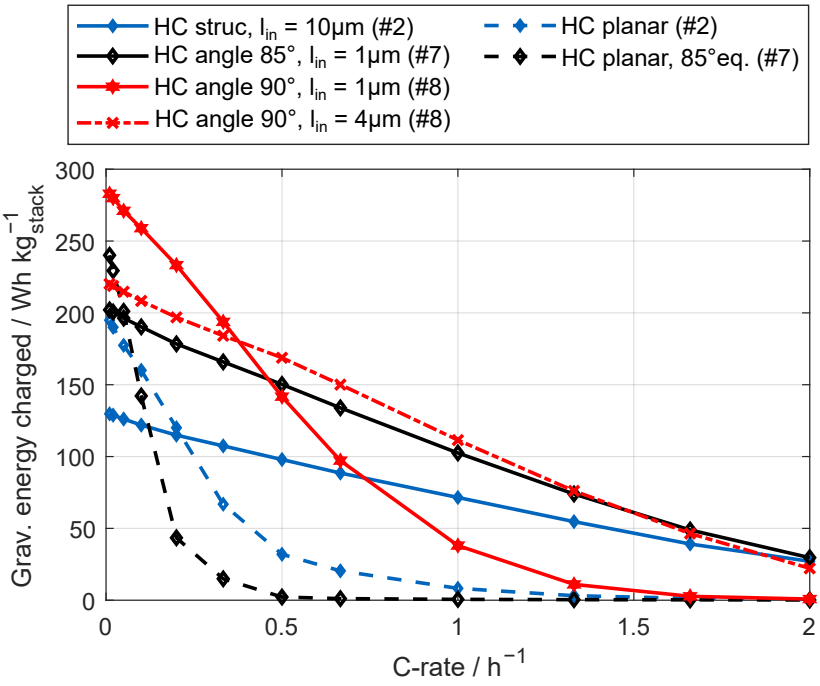

Figure 8. Evolution of the gravimetric energy density $E_{gr,ch}$ rate capability for selected sensitivity studies of geometric parameters. The structured designs for the selected studies are additionally compared to their planar equivalents as introduced in Figure 2. The HC #2 cell design and #7 HC angle design ($\alpha = 85°$) were selected to visualize the positive impact of the reduction in the inactive width l_{in} from 10 µm to 1 µm, as well as the influence of the structure angle of $\alpha = 85°$. The results of study #8 allow us to visualize the impact of the current constriction.

In addition to the visualization of the constriction effect, Figure 8 provides an overview of the development of energy density depending on geometric cell design. A comparative analysis of studies #2, #7, and #8 is provided in Figure 8, highlighting the critical role of geometric design on cell performance. This analysis includes both structured and equivalent planar designs. In particular, study #7 shows significant improvements by reducing the inactive width l_{in} from 10 µm to 1 µm and setting the angle to $\alpha = 85°$. In contrast, study #8 shows that further extreme modifications by laser ablation—resulting in $\alpha = 90°$ and l_{in}—do not improve the rate capability, thereby revealing the limits of structural design improvements. Notably, the structured cells exhibit a significant increase in rate capability compared to their planar counterparts.

In summary, the simulations indicate that hybrid cells with a ceramic LLZO SE separator and PEO/LiTFSI SPE in the composite cathode can benefit from laser-ablated structures. While these structures add volume and mass compared to planar cell design, reducing energy density at low rates, they significantly enhance rate capability by shortening diffu-

sion pathways and increasing the surface area at the SPE | LLZO interface, thus reducing polarization. Optimizing the inactive width l_{in} and structure angle α shows potential for further improvements. However, extreme geometries may decrease the rate capability due to increased polarization. The next section will discuss the practical relevance of these findings, focusing on specific capacity and energy density, alongside the prospects and challenges of implementing structured designs.

3.2.3. Influence of Material Transport Parameters

In the model-based study of Clausnitzer et al. [29], the authors found that a structured composite cathode cell design did not significantly improve performance when using a single inorganic SE with properties similar to LLZO. In addition to the results presented so far in this study, this indicates a material dependence of the effect of geometric structures on cell performance. Therefore, this section examines the influence of improved polymer transport parameters on the rate capability of structured cell designs, specifically evaluating whether such designs offer advantages beyond the previously used PEO/LiTFSI SPE in systems with less severe ion transport limitations. Based on our previous study that reviewed the literature and established state-of-the-art transport parameter ranges for an SPE combined with an LLZO SE, optimal values were selected for key SPE parameters in the Ω_{pos} domain [42]: the diffusivity $D_{Li,SPE}$, the ionic conductivity $\kappa_{Li,SPE}$, and the transference number t^+. Additionally, the exchange current density at the SPE | LLZO phase boundary Ω_{phb} was adjusted. The specific parameter changes are detailed in Table 3.

Table 3. Electrochemical parameter variations based on the parameter ranges identified from the literature for studying the impact of improved material parameters in structured cell designs. A detailed description of the chosen parameters is presented in our previous study [42].

Parameter	Unit	Reference	Improved	Source
$\kappa_{Li,SPE}$	$S\,m^{-1}$	0.12	0.22	[15]
$D_{Li,SPE}$	$m^2\,s^{-1}$	7.88×10^{-12}	1×10^{-11}	[6]
t_+^{SPE}	-	0.086	0.9	*
$i_{0,\Omega_{phb}}$	$A\,m^{-2}$	1.07	15	[49,52]

* development towards single-ion conducting SPE.

Geometric parameter studies #4 and #7 were re-simulated using enhanced transport parameters, focusing on designs with $l_{in} = 1\,\mu m$ and two different angles, $\alpha = 70°$ and $\alpha = 85°$. Figure 9b compares the rate dependency of $E_{gr,ch}$ for these structured designs and their planar counterparts, each with improved electrochemical parameterization. The maximum theoretical energy density for each design is identical to the results of the sensitivity studies since the same cathode morphology and geometric cell designs are used. Consequently, the observed C/100 gravimetric energy densities in Figure 9b closely match those in Figures 6b and 8.

As depicted in Figure 9b, the trend of improved performance in structured designs compared to their planar equivalents is consistent with previous findings using the "strong transport" limited parameterization. In both test cases, structured designs exhibit an enhanced rate capability, as indicated by a reduced slope in the curve. Notably, lower transport limitations cause the crossing points between structured and planar curves to shift to higher c-rates. For instance, in study #7, with a structure angle of 85°, the crossing point shifts from C/20 in the case of the original parameterization (see Figure 8, black lines) to 1C in the case of improved SPE transport properties. In study #4, the crossing point advances to 3.3C. This indicates that the crossing point's position along the c-rate axis depends on material properties. For improved SE material parameters, performance benefits due to structuring can only be expected at higher c-rates. This indicates that structuring could be particularly beneficial for applications requiring high charging rates. The best trade-off

between energy density and rate capability in this study is observed with a structure angle of 85° and an LLZO margin of 1 µm.

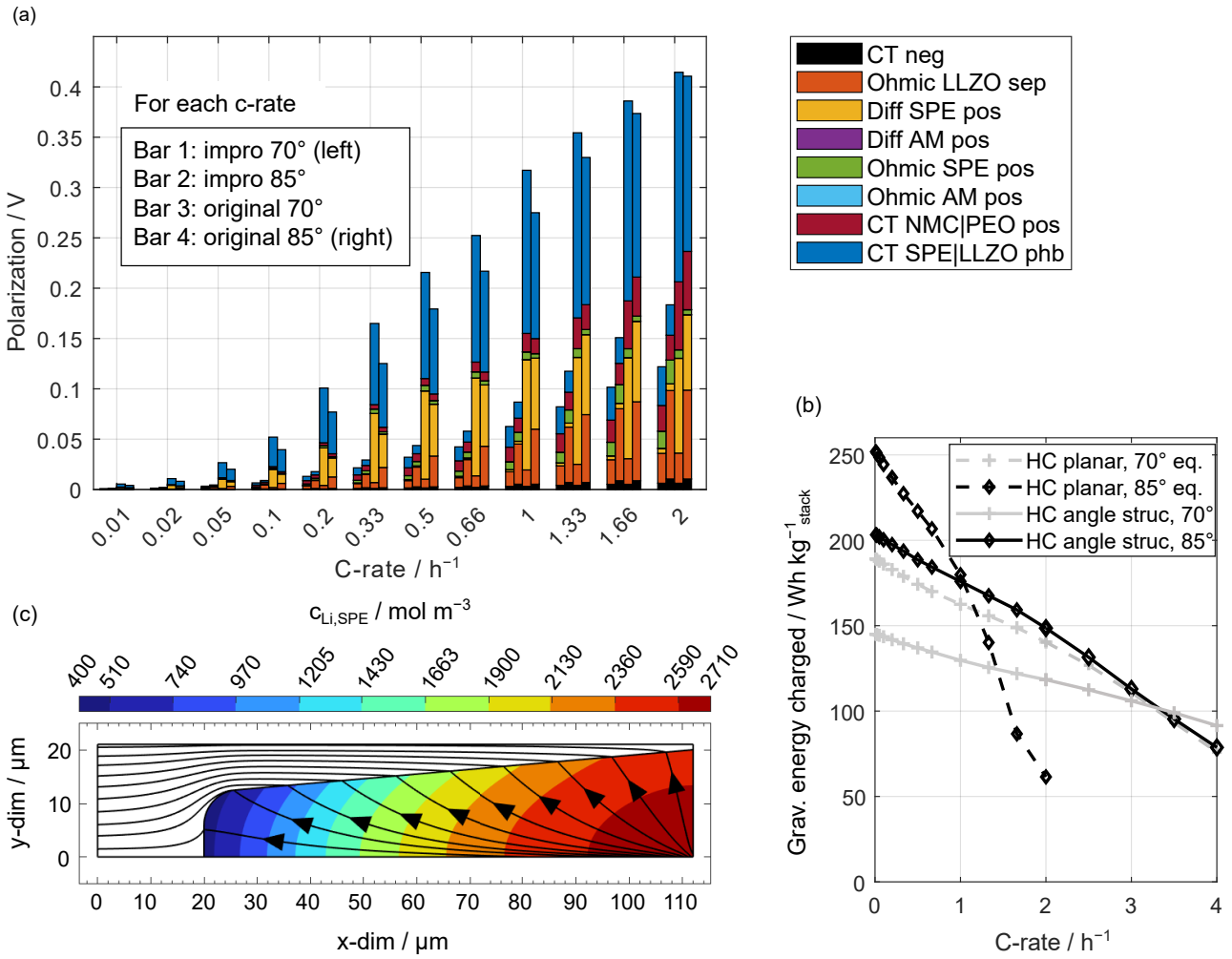

Figure 9. Performance evaluation of structured and planar cell design for improved SPE transport and LLZO | SPE charge transfer parameters, as listed in Table 3. The geometric designs of study #4 and #7 are chosen with an inactive width of $l_{in} = 1\,\mu m$ and a structure angle $\alpha = 70°$ and $\alpha = 85°$, respectively. (**a**) A comparison of the polarization for the two different designs with improved SPE and original parameterization. The polarization is captured at EoC for different c-rates. (**b**) The gravimetric energy density rate capability for cell designs #4 and #7 with improved SPE transport parameters. (**c**) A 2D visualization of concentration gradients of $c_{Li,SPE}$ with improved SPE parameters for the structured design of study #7 at an EoC of a 1C charge. Streamlines indicate the direction of the Li-ion flux in the SPE phase in the cathode and the LLZO separator phase. Since the concentration in the LLZO phase is constant, only the concentration profile in the SPE phase in the cathode was colored.

In general, the rate capability of all designs clearly improved with improved transport parameters. But in more detail, the rate capability behavior of the structured design with $\alpha = 70°$ clearly differs from that of the $\alpha = 85°$ design, as indicated by the different slopes. In contrast, the slopes when using the original parameterization were nearly identical (see Figure 6b). The reason for the increased rate capability in the case of $\alpha = 70°$ can be identified by analyzing individual polarization fractions in Figure 9a. With the improved SPE transport parameters, the total polarization of the $\alpha = 70°$ cell design, shown by the far-left bar, is lower than that of the $\alpha = 85°$ design, shown by the second left bar. This trend is contrary to that observed for the original parameterization, as shown by the second

right and far-right bars, and can be attributed to the change in SPE diffusion polarization (yellow). Due to the improved SPE parameters, the ionic transport in the LLZO separator (orange) becomes the major polarization effect.

The reduced diffusion limitation in the SPE phase in Ω_{pos} significantly alters the lithium-ion distribution within the SPE, when comparing the results in Figure 9c with Figure 4c. Enhanced SPE transport parameters cause a more pronounced concentration gradient in the x-direction from the current collector side toward the narrow region of the structure, resulting in an increased mean lithium-ion concentration along the Ω_{phb} boundary. In contrast, with the original parameterization shown in Figure 4c, the concentration gradient develops instead in the y-direction, leading to low concentrations distributed along the entire Ω_{phb} boundary. As the charge transfer resistance at Ω_{phb} decreases with higher SPE lithium concentration, the improved lithium-ion concentration distribution along the interface Ω_{phb} enhances the charge transfer at the boundary leading to lower polarization.

In summary, improving the SPE material's transport parameters generally reduced total polarization and enhanced rate capability, regardless of the cell's geometric design. Notably, a specific c-rate was identified where the structured design outperformed the planar one, with this crossing point shifting to higher c-rates with improved parameters. This metric could guide the choice of geometric cell design for specific applications. Additionally, the p3D model demonstrated that enhanced lithium-ion transport due to diffusion in the SPE phase improves charge transfer at the SPE | LLZO interface due to its dependence on lithium-ion concentration.

4. Assessment of the Practical Relevance of Structured Composite Cathodes by Comparison with Benchmarks from the Literature

Randau et al. [3] benchmarked the performance of SSBs by analyzing the literature data from existing experimental cells. The presented Ragone plots give valuable information about the relationship between energy density and rate performance that could be identified for different SE materials. Based on state-of-the-art liquid electrolyte lithium-ion batteries, a target range of a minimum of 250 Wh kg^{-1} gravimetric energy density and cycling rate greater than 1C was defined for SSBs. These indicators were also used to analyze the charging performance of hybrid cells at elevated temperatures between 50 °C and 100 °C containing an inorganic SE in combination with a polymer electrolyte, as well as cells containing only a polymer electrolyte. The literature data for seven different polymer-containing cells result in gravimetric energy densities between 90 Wh kg^{-1} and 290 Wh kg^{-1}, five of which have energy densities below 170 Wh kg^{-1} [53–59]. At a cycle rate of 1C, the cells reached energy densities between 90 Wh kg^{-1} and 110 Wh kg^{-1}. These data are used in the following to discuss the practical relevance of the performance achieved for the simulated cells with a structured design.

In this study, optimal performance in energy density and rate capability was achieved with a minimal inactive width of $l_{in} = 1$ µm and a structure angle of $\alpha = 85°$ (study #7; see Table 2). Using state-of-the-art PEO/LiTFSI material parameters, the maximum energy density reached 200 Wh kg^{-1} at C/100 and approximately 100 Wh kg^{-1} at 1C. Notably, this study incorporates an additional 20% mass from the 10 µm thick current collectors into the energy density calculation, unlike Randau et al. Without this mass, energy density for design #7 increases to 253 Wh kg^{-1} at C/100 and 128 Wh kg^{-1} at 1C. Despite limited ionic transport in the selected SPE parameters, the structured cell design demonstrated improved charging performance over a planar design. However, direct comparison with the literature is challenging due to varying polymer electrolytes and unreported transport and charge transfer parameters.

An improvement of the ionic transport and charge transfer parameters within their currently known parameter range further boosts the rate capability of the analyzed structured hybrid cell design. A gravimetric energy density for design #7 of 220 Wh kg^{-1} at 1C was reached in the simulation study, which is approximately 87% of the C/100 energy

density value. At a high-rate 4C condition, at least an energy density of 100 Wh kg^{-1} was achieved. In comparison, the best rate capability for polymer-containing cells, according to the Ragone plot in Randau et al.'s work, was achieved in the studies by Bouchet et al. [58] and Porcarelli et al. [57]. Bouchet et al. developed a single-ion polymer electrolyte based on block co-polymers. The rate test of a prototype cell with a Li-metal anode and a composite cathode containing 60 wt % lithium iron phosphate (LFP) AM and 32 wt % polymer electrolyte was conducted at 80 °C. At 1C, a capacity retention of around 82% based on a theoretical specific capacity of 170 mAh g^{-1} for LFP could be achieved, as well as a resulting energy density of around 90 Wh kg^{-1}. However, this is also due to the flat characteristic curve of the LFP cathode and the low cut-off voltage during discharge, whereby a large polarization of 1.5 V was tolerated [58]. Similarly, Porcarelli et al. synthesized a single-ion conducting triblock copolymer electrolyte and tested the rate capability in a prototype cell with a Li-metal anode and a composite cathode containing 65 wt % LFP and 20 wt % of single-ion conducting polymer. The observed polarization at C/2 and 70 °C was small, but some undiscussed limitations occurred, leading to an LFP capacity retention of 58% and a resulting energy density of 100 Wh kg^{-1} [57].

The simulation study achieved an energy density of 220 Wh kg^{-1} at 1C, approaching the target of 250 Wh kg^{-1} set by Randau et al. [3]. However, this result is constrained by the limited upper voltage cut-off of 4 V, imposed due to the reported decomposition of PEO/LiTFSI at higher cathode potentials [44,45]. By extending the voltage window to 4.3 V for nickel-rich CAMs and using suitable SPEs with enhanced electrochemical stability, further increases in specific capacity and energy density could be expected.

Furthermore, the cathode morphology in the simulation study is not optimized for a high-energy or high-power design. By increasing the CAM volume fraction ε_{AM} and decreasing the SPE volume fraction ε_{SPE}, a higher energy density at a low c-rate is expected, but the resulting increase in the tortuosity factor τ in the composite cathode could deteriorate the rate capability.

Up to this point, it could be shown that a well-derived structured geometrical design could significantly increase the rate capability and energy density of a hybrid SSB containing two different types of SE. Additionally, it could be shown that ionic transport and charge transfer parameters can significantly shift the point from which a structured cell design outperforms its planar equivalent. Therefore, the impact of the material choice of the two SEs in the hybrid system shows up as a decisive factor in the question of whether a structured design could increase the charging performance for a known application scenario. Additionally, to the best of the authors' knowledge, there are no data available that report on the aging behavior of structured SSB cells, which will also be a decisive factor for practical relevance. Finally, it should be mentioned that geometrical structuring, in general, comes with an additional process step in the manufacturing route, which could increase battery cost.

5. Conclusions

This study addresses the research gap in understanding the impact of laser-ablated geometric structures on the charging performance of hybrid SSBs. First, a p3D modeling approach specifically tailored for structured hybrid SSBs was implemented and parameterized, including a PEO/LiTFSI SPE in the cathode domain and an LLZO ceramic SE as the separator. The charge transfer at the LLZO|SPE interface was considered with BV-like kinetics, as introduced and discussed in our previous publication, and here transferred to a 2D model implementation [42].

Second, a basic geometric structure design was derived from the literature and compared to the "classical" planar cell design by analyzing the specific capacity $Q_{sp,ch}$, the gravimetric energy density $E_{gr,ch}$ and significant polarization contributions under varying charging rates up to 2C. Significant rate capability improvements in terms of $Q_{sp,ch}$ and $E_{gr,ch}$ were obtained with a structured design compared to a planar design. The two main reasons for improvement were identified, namely the reduction in the large polarization

contributions from SPE diffusion and charge transfer at the LLZO | SPE interface. The geometric structure shortens ionic pathways in the SPE phase and extends the length of the LLZO | SPE boundary, which reduces charge transfer polarization. A trade-off between improving the specific capacity $Q_{sp,ch}$ and increasing the weight and volume $E_{gr,ch}$ exists, as the structured design leads to higher material fractions of LLZO.

Third, the sensitivity of the geometric structure parameters towards their impact on charging performance was analyzed with the goal of minimizing additional inactive LLZO SE amounts and maintaining or improving AM utilization. Variation in the inactive width l_{in} and the structure angle α showed potential for further improvements. The best trade-off of the simulated geometries between high energy densities at low rates and good rate capability was obtained for $l_{in} = 1\,\mu m$ and $\alpha = 85°$. However, more extreme geometries with $\alpha = 90°$ and $l_{in} = 1\,\mu m$ decrease the rate capability due to increased polarization. The polarization within the LLZO domain Ω_{sep} increases with increasing α, as the current in the narrower LLZO region becomes more constricted, leading to higher current densities and local polarization. This leads to a trade-off between reducing the diffusion polarization in the SPE and increasing the ohmic polarization in the LLZO.

Fourth, the generality of the results obtained above was investigated by analyzing the same structured cell designs but with improved SPE parameters. Consistent with previous findings, improved performance was obtained for structured designs compared to their planar equivalents. Specifically, lower transport limitations cause the crossing points between the structured and the planar energy density curves to shift to higher rates, suggesting that structuring is particularly beneficial for applications requiring high charge rates. Consistent with the original parameterization, the optimal balance between energy density and rate capability was observed with a structure angle of 85° and an LLZO margin of 1 µm.

Finally, the practical relevance of these results was discussed in the context of the state-of-the-art literature. In the best case, an energy density at 1C of $128\,Wh\,kg^{-1}$ with the original parameterization, and $220\,Wh\,kg^{-1}$ with improved SPE parameters, was achieved for structured cell design, closely approaching the target of $250\,Wh\,kg^{-1}$ set by Randau et al. [3]. This highlights that the material parameters of the two SEs have a high impact on absolute numbers of performance parameters. Regarding the practical relevance, this emerges as a critical factor in determining whether a structured design could improve the charging performance for a known application scenario.

Future studies can connect to this study by performing a detailed optimization study based on the here shown high sensitivity of geometric parameters on performance indicators. In addition to that, further studies should research the aging behavior of structured SSB cells, which will also be a decisive factor for practical relevance. The analysis of additional process costs would be necessary to evaluate the practical relevance from an economic point of view.

Author Contributions: Conceptualization, M.S.; methodology, M.S.; formal analysis, M.S. and A.D.; investigation, M.S., A.D. and A.F.; resources, A.J.; data curation, M.S. and A.D.; writing—original draft preparation, M.S.; writing—review and editing, M.S., A.D., A.F. and A.J.; visualization, M.S.; supervision, A.J.; project administration, M.S. and A.J.; funding acquisition, A.J. All authors have read and agreed to the published version of the manuscript.

Funding: This research is funded by the Bavarian Ministry of Economic Affairs, Regional Development and Energy within the research project "Industrialisierbarkeit von Festkörperelektrolytzellen".

Data Availability Statement: Data are available upon request.

Acknowledgments: The authors are thankful for fruitful discussions with Johannes Kriegler, the members of the TUMint Energy Research GmbH, and the colleagues at the chair of Electrical Energy Storage Technology.

Conflicts of Interest: Author Maximilian Scheller was employed by the company TUMint Energy Research GmbH. The remaining authors declare that the research was conducted in the absence of any commercial or financial relationships that could be construed as a potential conflict of interest.

Acronyms

CM	celluluse nanofibers + multi-walled carbon nanotubes
LATP	lithium aluminum titanium phosphate
LFP	lithium iron phosphate
LLZO	lithium lanthanum zirconium oxide, Li7La3Zr2O12
LPSCL	lithium phosphorus sulfur chloride
Li	lithium
MEEP	poly(bis-(methoxyethoxyethoxy)phosphazene)
NCA	lithium nickel cobalt aluminum oxide
NMC	lithium nickel manganese cobalt oxide
AM	active material
BV	Butler–Volmer
CAM	cathode active material
CC	current collector
DFN	Doyle–Fuller–Newman
EoC	end-of-charge
HC	high-capacity
ISE	inorganic solid electrolyte
LIB	lithium-ion battery
PEO	poly(ethyleneoxide)
SE	solid electrolyte
SPE	solid-polymer electrolyte
SSB	solid-state battery
p2D	pseudo-two-dimensional
p3D	pseudo-three-dimensional
qOCP	quasi open-circuit potential

Roman Symbols

c	concentration, $\mathrm{mol\,m^{-3}}$
D	diffusivity, $\mathrm{m^2\,s^{-1}}$
d	thickness, x-axis, µm
$\frac{\partial U_{\mathrm{eq}}}{\partial T}$	entropic coefficient, $\mathrm{mV\,K^{-1}}$
E	energy density, $\mathrm{Wh\,kg^{-1}}$
U_{eq}	equilibrium potential, V
$\mathcal{F}$	Faraday's constant, 96,485 $\mathrm{A\,s\,mol^{-1}}$
I	current, A
i	current density, $\mathrm{A\,m^{-2}}$
i_0	exchange current density, $\mathrm{A\,m^{-2}}$
l	length, y-axis, µm
m	mass, kg
Q	gravimetric capacity, $\mathrm{mAh\,g^{-1}}$
$\mathcal{R}$	universal gas constant, 8.314 $\mathrm{J\,mol^{-1}\,K^{-1}}$
R_{p}	particle radius, m
T	temperature, K
t_+	transference number, no unit
V	volume, $\mathrm{m^3}$
J	molar flux, $\mathrm{mol\,m^{-2}\,s^{-1}}$

Greek Symbols

α	structure angle, °
α_{ct}	charge transfer coefficient, no unit
χ	stoichiometry, no unit
ε	volume fraction, no unit
η	overpotential, V
κ	ionic conductivity, $\mathrm{S\,m^{-1}}$

Ω	model domain
φ	electrical potential, V
σ	electronic conductivity, S m^{-1}
τ	tortuosity, no unit

Subscripts & Superscripts

abs	absolute
add	additional
app	applied
ave	average
b	bottom
ch	charge, simulation
eff	effective
gr	gravimetric, related to stack mass
in	inactive
max	maximum
phb	phase boundary SPE | LLZO
vol	volumetric
pos	positive electrode
pr	practical
sep	separator
sp	specific, related to electrode mass
st	structure
stack	cell stack with current collectors
surf	surface
t	top
th	theoretical
tot	total
v	volumetric

Appendix A. Model Equations and Parameters

Table A1. Equations for the p3D model. Here, ∇ describes the spatial gradient in the real 2D dimension, and $\frac{\partial}{\partial r}$ is the spatial gradient in the pseudo-dimension, along the radius of the active material particles.

Domain	Type	Equation
General	Spatial gradients	$\nabla = (\frac{\partial}{\partial x}\,,\ \frac{\partial}{\partial y})^{\intercal}$
	Effective transport correction	$D^{\text{eff}}_{\text{Li, SPE}} = \frac{\varepsilon_{\text{SE}}}{\tau}\, D_{\text{Li, SPE}},\ \kappa^{\text{eff}}_{\text{Li, SPE}} = \frac{\varepsilon_{\text{SE}}}{\tau}\, \kappa_{\text{Li, SPE}},\ \sigma^{\text{eff}}_{\text{s}} = \frac{\varepsilon_{\text{AM}}}{\tau}\, \sigma_{\text{s}}$
Li	Potentials	$\varphi_s = 0$
	Kinetics	$i_{\text{loc}}(y,t) \;=\; i_0(y,t)\Big[exp\Big(\frac{\alpha_{\text{ct}}\,\mathcal{F}\,\eta(y,t)}{\mathcal{R}\,T}\Big) - exp\Big(-\frac{\alpha_{\text{ct}}\,\mathcal{F}\,\eta(y,t)}{\mathcal{R}\,T}\Big)\Big]\big\vert_{x=x_0}$
LLZO	Mass balance	$\frac{\partial c_{\text{Li, LLZO}}(x,y,t)}{\partial t} \;=\; 0$
	Charge balance	$\nabla\, i_{\text{LLZO}}(x,y,t) \;=\; 0$
	Potentials	$\nabla\, \varphi_{\text{LLZO}}(x,y,t) \;=\; -\frac{i_{\text{LLZO}}(x,y,t)}{\kappa_{\text{LLZO}}}$
Cathode	Mass balance	$\frac{\partial c_{\text{Li, SPE}}(x,y,t)}{\partial t} \;=\; \nabla\Big(D^{\text{eff}}_{\text{Li, SPE}}\nabla c_{\text{Li, SPE}}(x,y,t) + \frac{i_{\text{SPE}}(x,y,t)\, t^{\text{SPE}}_{+}}{\mathcal{F}}\Big)$
		$\frac{\partial\, c_{\text{s}}(x,y,t,r)}{\partial t} \;=\; \frac{1}{r^2}\frac{\partial}{\partial r}\Big(D_{\text{s}} r^2 \frac{\partial\, c_{\text{s}}(x,y,t,r)}{\partial r}\Big)$
	Charge balance	$\nabla\, i_{\text{SPE}}(x,y,t) + \nabla\, i_{\text{s}}(x,y,t) \;=\; 0 \quad \text{with} \quad \nabla\, i_{\text{s}}(x,y,t) \;=\; -\frac{3\varepsilon_{\text{AM}}}{R_{\text{p}}}\, i_{\text{loc}}(x,y,t)$
	Potentials	$\nabla\, \varphi_{\text{SPE}}(x,y,t) \;=\; -\frac{i_{\text{SPE}}(x,y,t)}{\kappa^{\text{eff}}_{\text{SPE}}} + \frac{2\,\mathcal{R}\,\mathcal{F}}{F}\,(1 - t^{\text{SPE}}_{+})\,\Big(1 + \frac{d\, ln f_{\pm}}{d\, ln\, c_{\text{Li, SPE}}(x,y,t)}\Big)\,\nabla\, ln\, c_{\text{Li, SPE}}(x,y,t)$
		$\nabla\, \varphi_{\text{s}}(x,y,t) \;=\; -\frac{i_{\text{s}}(x,y,t)}{\sigma^{\text{eff}}_{\text{s}}} \quad \text{with} \quad i_{\text{app}}(t) \;=\; i_{\text{s}}(x,y,t) + i_{\text{SPE}}(x,y,t) \quad \forall\, x,y,t$
	Kinetics	$i_{\text{loc}}(x,y,t) \;=\; i_0(x,y,t)\Big[exp\Big(\frac{\alpha_{\text{ct}}\,\mathcal{F}\,\eta(x,y,t)}{\mathcal{R}\,T}\Big) - exp\Big(-\frac{\alpha_{\text{ct}}\,\mathcal{F}\,\eta(x,y,t)}{\mathcal{R}\,T}\Big)\Big]$

Table A2. Reference parameterization of the p2D model with an additional SPE interlayer and AM particle coating, separated for each model domain.

Parameter	Symbol	Unit	LLZO Ω_{sep}	Composite Cathode Ω_{pos}	Ref.
Microstructure					
Particle radius	R_p	µm		1	
Active material fraction	ε_{AM}	vol.%		66	[25]
SE material fraction	ε_{SE}	vol.%	100	31	[25]
Cond. additives	ε_{add}	vol.%		3	
Tortuosity	τ			4	[46]
Transport [a]					
Diffusivity SE	D_{SE}	$m^2\,s^{-1}$		7.88×10^{-12}	[6]
Ionic conductivity SE	κ_{SE}	$S\,m^{-1}$	0.1	0.12	[15,50]
Diffusivity AM	D_{AM}	$m^2\,s^{-1}$		5×10^{-13}	[60]
Electronic conductivity	σ	$S\,m^{-1}$		100	non-limiting
Transference number	t_+		1	0.086	[15]
Thermodynamic factor	TDF		1	3.34	[15,17]
Kinetics					
AM exchange current	$i_{0,AM}$	$A\,m^{-2}$	$1000\|_{x=x_0}$ [b]	$0.30\|_{r=R_p}$	[61,62]
phb exchange current	$i_{0,\Omega_{phb}}$	$A\,m^{-2}$		$1.07\|_{\Omega_{phb}}$	[49]
Transfer coefficient	α_{ct}			0.5 [c]	
Cell					
NMC equilibrium potential	U_{eq}	V	$0\|_{x=x_0}$	meas.	[51]
Stoichiometry χ 100% SoC	χ_1			0.474 [d]	
0% SoC	χ_0			0.99	
Max. concentration	$c_{s,max}$	$mol\,m^{-3}$		50,066	
Concentration-dependent parameters [e]			**Argument/Unit**	**Function/Unit**	
PEO I LLZO charge transfer resistance $R_{ct,\Omega_{phb}}$			$c_{Li,SPE}\,/\,mol\,m^{-3}$	$1.048 \cdot c_{Li,SPE}^{-0.4986}\,/\,\Omega\,m^2$	[49]
SPE transport parameters			see Pesko et al. [15] for analytical expressions		

[a] SPE transport parameters are concentration-dependent and here evaluated at $c_{Li,SPE}$ =1960 $mol\,m^{-3}$. [b] Negligibly small interface resistance, if high external loads are applied and no contamination layers are present [61]. [c] Assuming symmetric charge transfer for all reactions. [d] The given stoichiometric value corresponds to an NMC-811 equilibrium potential of 4 V. [e] Analytic functions for the electrolyte are physically not interpretable. The output value is to be interpreted in the unit given in the table or in the literature reference.

Table A3. Additional parameters in relation to the specific capacity and energy density, as calculated according to Table A4 for all simulated geometric variations presented in Table 2.

Study #	Study Name	Cell Parameters			
		Normalized Total Cell Volume	Normalized Total Cell Mass	Theor. Areal Capacity mAh cm^{-2}	Theor. Energy Density E_{gr}/Wh kg^{-1}
#1	BASE	1	1	2.26	118.2
#2	High Capacity (HC)	1.28	1.27	2.88	129.7
#3	HC inactive 7 µm	1.16	1.14	3.17	144.7
	HC inactive 4 µm	1.04	1.01	3.52	163.6
	HC inactive 1 µm	0.92	0.88	3.94	187.3
#4	HC angle 1	1.17	1.15	2.64	143.9
#5	HC angle 2	1.09	1.06	3.00	155.9
#6	HC angle 3	1.00	0.96	3.54	173.0
#7	HC angle 4	0.87	0.82	4.50	202.1
#8	HC angle 5	0.66	0.59	7.30	282.9

Table A4. Calculation of specific capacity and energy density for an out-of-plane (z-direction) thickness $t_z = 1\,\mathrm{m}$.

Domain	**Gravimetric Density ρ/g cm^{-3}**	**Layer Thickness t/µm**	**Volume V/cm^3**	**Mass m/g**
Copper CC	8.96	10	$V_{\mathrm{CC,a}} = t_{\mathrm{CC,a}} \cdot l_y \cdot t_z$	$m_{\mathrm{CC,a}} = \rho_{\mathrm{CC,a}} \cdot V_{\mathrm{CC,a}}$
Aluminum CC	2.7	10	$V_{\mathrm{CC,c}} = t_{\mathrm{CC,c}} \cdot l_y \cdot t_z$	$m_{\mathrm{CC,c}} = \rho_{\mathrm{CC,c}} \cdot V_{\mathrm{CC,c}}$
Lithium metal anode	0.53	5	$V_{\mathrm{Li}} = t_{\mathrm{Li}} \cdot l_y \cdot t_z$	$m_{\mathrm{Li}} = \rho_{\mathrm{Li}} \cdot V_{\mathrm{Li}}$
LLZO separator Ω_{sep}	5.07	20	$V_{\mathrm{sep}} = t_{\mathrm{sep}} \cdot l_y \cdot t_z$	$m_{\mathrm{sep}} = \rho_{\mathrm{sep}} \cdot V_{\mathrm{sep}}$
LLZO structure $\Omega_{st,\mathrm{LLZO}}$	5.07	-	$V^{meas.}_{st,\mathrm{LLZO}}$	$m_{st,\mathrm{LLZO}} = \rho_{\mathrm{LLZO}} \cdot V^{meas.}_{st,\mathrm{LLZO}}$
Cathode structure Ω_{pos}	$\rho_{\mathrm{pos}} = \frac{1}{\frac{\omega_{\mathrm{AM}}}{\rho_{\mathrm{AM}}} + \frac{\omega_{add}}{\rho_{add}} + \frac{\omega_{\mathrm{SPE}}}{\rho_{\mathrm{SPE}}}} = 3.52$	-	$V^{meas.}_{\mathrm{pos}}$	$m_{\mathrm{pos}} = \rho_{\mathrm{pos}} \cdot V^{meas.}_{\mathrm{pos}}$
Stack calculation				
Total volume	$V_{\mathrm{stack}} = V_{\mathrm{CC,a}} + V_{\mathrm{CC,c}} + V_{\mathrm{Li}} + V_{\mathrm{sep}} + V^{meas.}_{\mathrm{st,LLZO}} + V^{meas.}_{\mathrm{pos}}$			
Total mass	$m_{\mathrm{stack}} = m_{\mathrm{CC,a}} + m_{\mathrm{CC,c}} + m_{\mathrm{Li}} + m_{\mathrm{sep}} + m_{\mathrm{st,LLZO}} + m_{\mathrm{pos}}$			
Cell equil. potential	$U_{\mathrm{eq}} = U_{OCP}\left(\frac{\iiint_{\mathrm{pos}} \frac{c_{s,ave}}{c_{s,max}}\, d\mathrm{pos}}{\iiint_{\mathrm{pos}} 1\, d\mathrm{pos}}\right)$			
Capacity charge	$Q_{\mathrm{ch}} = \int_{t_0}^{t_{EoC}} I_{app}\, dt$			
Energy charge	$E_{\mathrm{ch}} = \int_{t_0}^{t_{EoC}} U_{\mathrm{eq}} \cdot I_{app}\, dt$			
Specific capacity	$Q_{\mathrm{sp,ch}} = \frac{Q_{\mathrm{ch}}}{m_{\mathrm{pos}}}$			
Gravimetric energy density	$E_{\mathrm{gr,ch}} = \frac{E_{\mathrm{ch}}}{m_{\mathrm{stack}}}$			
Volumetric energy density	$E_{\mathrm{vol,ch}} = \frac{E_{\mathrm{ch}}}{V_{\mathrm{stack}}}$			

Table A5. Calculation of individual polarization contributions for 2D model geometries for isotropic material parameters, adapted from Nyman et al. [37].

Parameter	**Equation**
Total current	$i_{\mathrm{tot}} = \iiint_{\mathrm{pos}} i_{\mathrm{v,pos}}\, d\mathrm{pos}$
Domain	
Diffusion SPE phase	$\frac{1}{i_{\mathrm{tot}}} \iiint_{\mathrm{pos}} \frac{2\mathcal{R}T}{\mathcal{F}} \left(1 + \frac{\partial \ln f_{\pm}}{\partial \ln c_{\mathrm{Li,SPE}}}\right)(1 - t_+) \left[\frac{1}{c_{\mathrm{Li,SPE}}} \left(\frac{\partial c_{\mathrm{Li,SPE}}}{\partial x}\, i_{\mathrm{SPE},x} + \frac{\partial c_{\mathrm{Li,SPE}}}{\partial y}\, i_{\mathrm{SPE},y}\right)\right] d\mathrm{pos}$
Diffusion AM particle	$\frac{1}{i_{\mathrm{tot}}} \iiint_{\mathrm{pos}} i_{\mathrm{v,pos}} \left(U_{\mathrm{eq,surf}} - U_{\mathrm{eq,ave}}\right) d\mathrm{pos}$
Ohmic LLZO	$\frac{1}{i_{\mathrm{tot}}} \iiint_{\mathrm{sep}} \frac{i^2_{\mathrm{LLZO},x} + i^2_{\mathrm{LLZO},y}}{\kappa_{\mathrm{eff}}}\, d\mathrm{sep}$
Ohmic AM Pos	$\frac{1}{i_{\mathrm{tot}}} \iiint_{\mathrm{pos}} \frac{i^2_{s,x} + i^2_{s,y}}{\sigma_{\mathrm{eff}}}\, d\mathrm{pos}$
Ohmic SPE Pos	$\frac{1}{i_{\mathrm{tot}}} \iiint_{\mathrm{pos}} \frac{i^2_{\mathrm{SPE},x} + i^2_{\mathrm{SPE},y}}{\kappa_{\mathrm{eff}}}\, d\mathrm{pos}$
CT reaction cathode	$\frac{1}{i_{\mathrm{tot}}} \iiint_{\mathrm{pos}} i_{v,\mathrm{pos}} \left(\varphi_s - \varphi_{\mathrm{SPE}} - U_{\mathrm{eq,surf}}\right) d\mathrm{pos}$
Boundary	
CT reaction anode	$\frac{1}{i_{\mathrm{tot}}} \int_{y_0}^{y_1} i_{\mathrm{LLZO}}(y) \left(\varphi_{\mathrm{Li}} - \varphi_{\mathrm{LLZO}} - U_{\mathrm{eq,Li}}\right) dy \,\big|_{x=x_0}$
CT PEO | LLZO	$\frac{1}{i_{\mathrm{tot}}} \oint_{\Omega_{\mathrm{phb}}} i_{n,\mathrm{phb}} \left(\varphi_{\mathrm{LLZO}} - \varphi_{\mathrm{SPE}}\right) d\Omega_{\mathrm{phb}}$

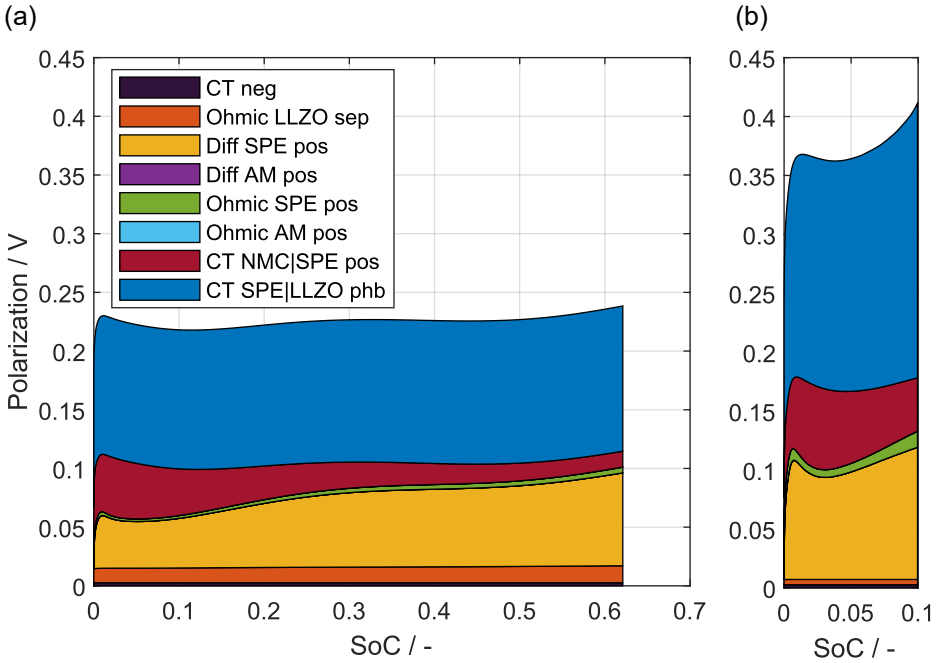

Figure A1. Transient course of single polarization contributions stacked on top of each other at 1C charging rate for the BASE structured design in (**a**) and the planar design in (**b**). Each colored section represents the transient behavior of the allocated share of polarization, as calculated in Table A5.

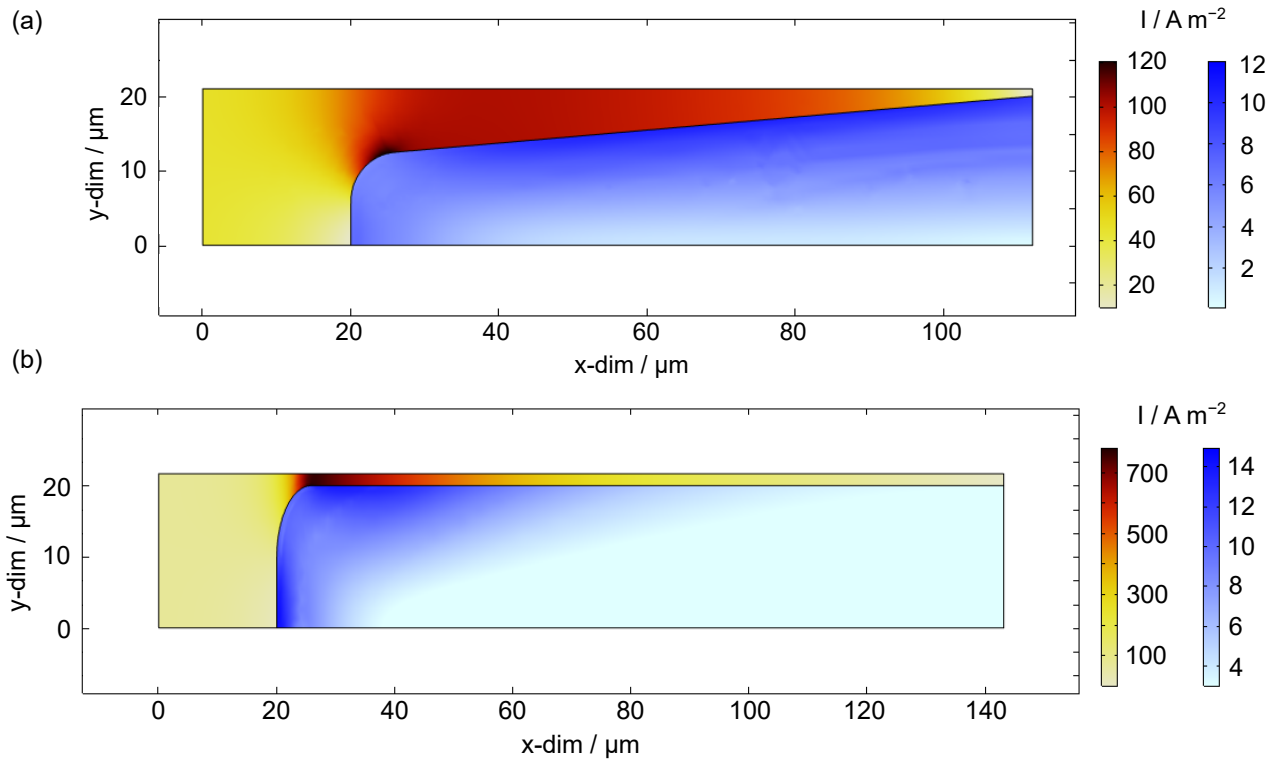

Figure A2. Electrolyte current density for (**a**) a structure angle of $\alpha = 85°$ (study #7) and for (**b**) a structure angle of $\alpha = 90°$ (study #8). Different colormaps for the LLZO domain Ω_{sep} and the cathode domain Ω_{pos} are used to visualize the different value ranges properly.

References

1. Blomgren, G.E. The Development and Future of Lithium Ion Batteries. *J. Electrochem. Soc.* **2017**, *164*, A5019–A5025. [CrossRef]
2. Kato, Y.; Hori, S.; Saito, T.; Suzuki, K.; Hirayama, M.; Mitsui, A.; Yonemura, M.; Iba, H.; Kanno, R. High-power all-solid-state batteries using sulfide superionic conductors. *Nat. Energy* **2016**, *1*, 652. [CrossRef]

3. Randau, S.; Weber, D.A.; Kötz, O.; Koerver, R.; Braun, P.; Weber, A.; Ivers-Tiffée, E.; Adermann, T.; Kulisch, J.; Zeier, W.G.; et al. Benchmarking the performance of all-solid-state lithium batteries. *Nat. Energy* **2020**, *5*, 259–270. [CrossRef]
4. Bachman, J.C.; Muy, S.; Grimaud, A.; Chang, H.H.; Pour, N.; Lux, S.F.; Paschos, O.; Maglia, F.; Lupart, S.; Lamp, P.; et al. Inorganic Solid-State Electrolytes for Lithium Batteries: Mechanisms and Properties Governing Ion Conduction. *Chem. Rev.* **2016**, *116*, 140–162. [CrossRef]
5. Zhao, Q.; Stalin, S.; Zhao, C.Z.; Archer, L.A. Designing solid-state electrolytes for safe, energy-dense batteries. *Nat. Rev. Mater.* **2020**, *5*, 229–252. [CrossRef]
6. Hallinan, D.T.; Balsara, N.P. Polymer Electrolytes. *Annu. Rev. Mater. Res.* **2013**, *43*, 503–525. [CrossRef]
7. Meng, Y.S.; Srinivasan, V.; Xu, K. Designing better electrolytes. *Science* **2022**, *378*, eabq3750. [CrossRef]
8. Ren, Y.; Danner, T.; Moy, A.; Finsterbusch, M.; Hamann, T.; Dippell, J.; Fuchs, T.; Müller, M.; Hoft, R.; Weber, A.; et al. Oxide–Based Solid–State Batteries: A Perspective on Composite Cathode Architecture. *Adv. Energy Mater.* **2023**, *13*, 710. [CrossRef]
9. Hitz, G.T.; McOwen, D.W.; Zhang, L.; Ma, Z.; Fu, Z.; Wen, Y.; Gong, Y.; Dai, J.; Hamann, T.R.; Hu, L.; et al. High-rate lithium cycling in a scalable trilayer Li-garnet-electrolyte architecture. *Mater. Today* **2019**, *22*, 50–57. [CrossRef]
10. Shi, C.; Hamann, T.; Takeuchi, S.; Alexander, G.V.; Nolan, A.M.; Limpert, M.; Fu, Z.; O'Neill, J.; Godbey, G.; Dura, J.A.; et al. 3D Asymmetric Bilayer Garnet-Hybridized High-Energy-Density Lithium-Sulfur Batteries. *ACS Appl. Mater. Interfaces* **2023**, *15*, 751–760. [CrossRef]
11. Beaupain, J.P.; Waetzig, K.; Otto, S.K.; Henss, A.; Janek, J.; Malaki, M.; Pokle, A.; Müller, J.; Butz, B.; Volz, K.; et al. Reaction of $Li_{1.3}Al_{0.3}Ti_{1.7}(PO_4)_3$ and $LiNi_{0.6}Co_{0.2}Mn_{0.2}O_2$ in Co-Sintered Composite Cathodes for Solid-State Batteries. *ACS Appl. Mater. Interfaces* **2021**, *13*, 47488–47498. [CrossRef] [PubMed]
12. Ihrig, M.; Ye, R.; Laptev, A.M.; Grüner, D.; Guerdelli, R.; Scheld, W.S.; Finsterbusch, M.; Wiemhöfer, H.D.; Fattakhova-Rohlfing, D.; Guillon, O. Polymer–Ceramic Composite Cathode with Enhanced Storage Capacity Manufactured by Field-Assisted Sintering and Infiltration. *ACS Appl. Energy Mater.* **2021**, *4*, 10428–10432. [CrossRef]
13. Ihrig, M.; Dashjav, E.; Laptev, A.M.; Ye, R.; Grüner, D.; Ziegner, M.; Odenwald, P.; Finsterbusch, M.; Tietz, F.; Fattakhova-Rohlfing, D.; et al. Increasing the performance of all-solid-state Li batteries by infiltration of Li-ion conducting polymer into LFP-LATP composite cathode. *J. Power Sources* **2022**, *543*, 231822. [CrossRef]
14. Sen, S.; Trevisanello, E.; Niemöller, E.; Shi, B.X.; Simon, F.J.; Richter, F.H. The role of polymers in lithium solid-state batteries with inorganic solid electrolytes. *J. Mater. Chem. A* **2021**, *9*, 18701–18732. [CrossRef]
15. Pesko, D.M.; Feng, Z.; Sawhney, S.; Newman, J.; Srinivasan, V.; Balsara, N.P. Comparing Cycling Characteristics of Symmetric Lithium-Polymer-Lithium Cells with Theoretical Predictions. *J. Electrochem. Soc.* **2018**, *165*, A3186–A3194. [CrossRef]
16. Stolz, L.; Homann, G.; Winter, M.; Kasnatscheew, J. The Sand equation and its enormous practical relevance for solid-state lithium metal batteries. *Mater. Today* **2021**, *44*, 9–14. [CrossRef]
17. Villaluenga, I.; Pesko, D.M.; Timachova, K.; Feng, Z.; Newman, J.; Srinivasan, V.; Balsara, N.P. Negative Stefan-Maxwell Diffusion Coefficients and Complete Electrochemical Transport Characterization of Homopolymer and Block Copolymer Electrolytes. *J. Electrochem. Soc.* **2018**, *165*, A2766–A2773. [CrossRef]
18. Gupta, A.; Sakamoto, J. Controlling Ionic Transport through the PEO-LiTFSI/LLZTO Interface. *Electrochem. Soc. Interface* **2019**, *28*, 63–69. [CrossRef]
19. Langer, F.; Palagonia, M.S.; Bardenhagen, I.; Glenneberg, J.; La Mantia, F.; Kun, R. Impedance Spectroscopy Analysis of the Lithium Ion Transport through the $Li_7La_3Zr_2O_{12}$/$P(EO)_{20}$ Li Interface. *J. Electrochem. Soc.* **2017**, *164*, A2298–A2303. [CrossRef]
20. Wurster, V.; Engel, C.; Graebe, H.; Ferber, T.; Jaegermann, W.; Hausbrand, R. Characterization of the Interfaces in $LiFePO_4$/PEO-LiTFSI Composite Cathodes and to the Adjacent Layers. *J. Electrochem. Soc.* **2019**, *166*, A5410–A5420. [CrossRef]
21. Li, Z.; Sha, W.X.; Guo, X. Three-Dimensional Garnet Framework-Reinforced Solid Composite Electrolytes with High Lithium-Ion Conductivity and Excellent Stability. *ACS Appl. Mater. Interfaces* **2019**, *11*, 26920–26927. [CrossRef] [PubMed]
22. Shen, H.; Yi, E.; Amores, M.; Cheng, L.; Tamura, N.; Parkinson, D.Y.; Chen, G.; Chen, K.; Doeff, M. Oriented porous LLZO 3D structures obtained by freeze casting for battery applications. *J. Mater. Chem. A* **2019**, *7*, 20861–20870. [CrossRef]
23. Shen, H.; Yi, E.; Heywood, S.; Parkinson, D.Y.; Chen, G.; Tamura, N.; Sofie, S.; Chen, K.; Doeff, M.M. Scalable Freeze-Tape-Casting Fabrication and Pore Structure Analysis of 3D LLZO Solid-State Electrolytes. *ACS Appl. Mater. Interfaces* **2020**, *12*, 3494–3501. [CrossRef]
24. Buannic, L.; Naviroj, M.; Miller, S.M.; Zagorski, J.; Faber, K.T.; Llordés, A. Dense freeze–cast $Li_7La_3Zr_2O_{12}$ solid electrolytes with oriented open porosity and contiguous ceramic scaffold. *J. Am. Ceram. Soc.* **2019**, *102*, 1021–1029. [CrossRef]
25. Kriegler, J.; Jaimez-Farnham, E.; Scheller, M.; Dashjav, E.; Konwitschny, F.; Wach, L.; Hille, L.; Tietz, F.; Zaeh, M.F. Design, production, and characterization of three-dimensionally-structured oxide-polymer composite cathodes for all-solid-state batteries. *Energy Storage Mater.* **2023**, *57*, 607–617. [CrossRef]
26. Habedank, J.B.; Kraft, L.; Rheinfeld, A.; Krezdorn, C.; Jossen, A.; Zaeh, M.F. Increasing the Discharge Rate Capability of Lithium-Ion Cells with Laser-Structured Graphite Anodes: Modeling and Simulation. *J. Electrochem. Soc.* **2018**, *165*, A1563–A1573. [CrossRef]
27. Kraft, L.; Habedank, J.B.; Frank, A.; Rheinfeld, A.; Jossen, A. Modeling and Simulation of Pore Morphology Modifications using Laser-Structured Graphite Anodes in Lithium-Ion Batteries. *J. Electrochem. Soc.* **2020**, *167*, 013506. [CrossRef]
28. Kriegler, J.; Hille, L.; Stock, S.; Kraft, L.; Hagemeister, J.; Habedank, J.B.; Jossen, A.; Zaeh, M.F. Enhanced performance and lifetime of lithium-ion batteries by laser structuring of graphite anodes. *Appl. Energy* **2021**, *303*, 117693. [CrossRef]

29. Clausnitzer, M.; Danner, T.; Prifling, B.; Neumann, M.; Schmidt, V.; Latz, A. Influence of Electrode Structuring Techniques on the Performance of All–Solid–State Batteries. *Batter. Supercaps* **2024**, *7*, e202300522. [CrossRef]
30. Ji, S.; Wang, X.; Li, K.; Huan, Y.; Ma, G.; Su, Y.; Wei, T. 3D Vertically Aligned Microchannel Three-Layer All Ceramic Lithium Ion Battery for High-Rate and Long-Cycle Electrochemical Energy Storage. *Small* **2022**, *18*, e2107442. [CrossRef]
31. Xu, R.; Liu, F.; Ye, Y.; Chen, H.; Yang, R.R.; Ma, Y.; Huang, W.; Wan, J.; Cui, Y. A Morphologically Stable Li/Electrolyte Interface for All-Solid-State Batteries Enabled by 3D-Micropatterned Garnet. *Adv. Mater.* **2021**, *33*, e2104009. [CrossRef] [PubMed]
32. Jangid, M.K.; Davis, A.L.; Liao, D.W.; Dasgupta, N.P. Improved Rate Capability in Composite Solid-State Battery Electrodes Using 3-D Architectures. *ACS Energy Lett.* **2023**, *8*, 2522–2531. [CrossRef]
33. Zekoll, S.; Marriner-Edwards, C.; Hekselman, A.K.O.; Kasemchainan, J.; Kuss, C.; Armstrong, D.E.J.; Cai, D.; Wallace, R.J.; Richter, F.H.; Thijssen, J.H.J.; et al. Hybrid electrolytes with 3D bicontinuous ordered ceramic and polymer microchannels for all-solid-state batteries. *Energy Environ. Sci.* **2018**, *11*, 185–201. [CrossRef]
34. Kriegler, J.; Finsterbusch, M.; Liang, Y.; Jaimez-Farnham, E.; Zaeh, M.F. A perspective on the design, manufacturing, and energy content of oxide all-solid-state batteries with scaffold-based composite cathodes. *J. Power Sources* **2024**, *596*, 234091. [CrossRef]
35. Bielefeld, A.; Weber, D.A.; Rueß, R.; Glavas, V.; Janek, J. Influence of Lithium Ion Kinetics, Particle Morphology and Voids on the Electrochemical Performance of Composite Cathodes for All-Solid-State Batteries. *J. Electrochem. Soc.* **2022**, *169*, 020539. [CrossRef]
36. Wu, S.; Zheng, H.; Wang, X.; Zhang, N.; Cheng, W.; Fu, B.; Chen, H.; Liu, H.; Duan, H. High-capacity, low-tortuosity $LiFePO_4$-Based composite cathode enabled by self-supporting structure combined with laser drilling technology. *Chem. Eng. J.* **2022**, *430*, 132810. [CrossRef]
37. Nyman, A.; Zavalis, T.G.; Elger, R.; Behm, M.; Lindbergh, G. Analysis of the Polarization in a Li-Ion Battery Cell by Numerical Simulations. *J. Electrochem. Soc.* **2010**, *157*, A1236. [CrossRef]
38. Doyle, M.; Fuller, T.F.; Newman, J. Modeling of Galvanostatic Charge and Discharge of the Lithium/Polymer/Insertion Cell. *J. Electrochem. Soc.* **1993**, *140*, 1526–1533. [CrossRef]
39. Newman, J.; Balsara, N.P. *Electrochemical Systems*, 4th ed.; The Electrochemical Society Series; Wiley: Hoboken, NJ, USA, 2021.
40. Wolff, N.; Röder, F.; Krewer, U. Model Based Assessment of Performance of Lithium-Ion Batteries Using Single Ion Conducting Electrolytes. *Electrochim. Acta* **2018**, *284*, 639–646. [CrossRef]
41. Toghyani, S.; Baakes, F.; Zhang, N.; Kühnelt, H.; Cistjakov, W.; Krewer, U. Model-Based Design of High Energy All-Solid-State Li Batteries with Hybrid Electrolytes. *J. Electrochem. Soc.* **2022**, *169*, 040550. [CrossRef]
42. Scheller, M.; Durdel, A.; Frank, A.; Kriegler, J.; Jossen, A. Impact of Polymer Interlayers on All-Solid-State Battery Performance Using a Physicochemical Modeling Approach. *J. Electrochem. Soc.* **2024**, *171*, 020509. [CrossRef]
43. Lu, B.; Song, Y.; Zhang, Q.; Pan, J.; Cheng, Y.T.; Zhang, J. Voltage hysteresis of lithium ion batteries caused by mechanical stress. *Phys. Chem. Chem. Phys. PCCP* **2016**, *18*, 4721–4727. [CrossRef] [PubMed]
44. Wetjen, M.; Kim, G.T.; Joost, M.; Appetecchi, G.B.; Winter, M.; Passerini, S. Thermal and electrochemical properties of PEO-LiTFSI-Pyr_{14}TFSI-based composite cathodes, incorporating 4 V-class cathode active materials. *J. Power Sources* **2014**, *246*, 846–857. [CrossRef]
45. Xia, Y.; Fujieda, T.; Tatsumi, K.; Prosini, P.P.; Sakai, T. Thermal and electrochemical stability of cathode materials in solid polymer electrolyte. *J. Power Sources* **2001**, *92*, 234–243. [CrossRef]
46. Minnmann, P.; Quillman, L.; Burkhardt, S.; Richter, F.H.; Janek, J. Editors' Choice—Quantifying the Impact of Charge Transport Bottlenecks in Composite Cathodes of All-Solid-State Batteries. *J. Electrochem. Soc.* **2021**, *168*, 040537. [CrossRef]
47. Mistry, A.; Grundy, L.S.; Halat, D.M.; Newman, J.; Balsara, N.P.; Srinivasan, V. Effect of Solvent Motion on Ion Transport in Electrolytes. *J. Electrochem. Soc.* **2022**, *169*, 040524. [CrossRef]
48. Mistry, A.; Srinivasan, V.; Steinrück, H.G. Characterizing Ion Transport in Electrolytes via Concentration and Velocity Profiles. *Adv. Energy Mater.* **2023**, *13*, 100260. [CrossRef]
49. Brogioli, D.; Langer, F.; Kun, R.; La Mantia, F. Space-Charge Effects at the $Li_7La_3Zr_2O_{12}$/Poly(ethylene oxide) Interface. *ACS Appl. Mater. Interfaces* **2019**, *11*, 11999–12007. [CrossRef]
50. Janek, J.; Zeier, W.G. A solid future for battery development. *Nature Energy* **2016**, *1*, 1167. [CrossRef]
51. Sturm, J.; Rheinfeld, A.; Zilberman, I.; Spingler, F.B.; Kosch, S.; Frie, F.; Jossen, A. Modeling and simulation of inhomogeneities in a 18650 nickel-rich, silicon-graphite lithium-ion cell during fast charging. *J. Power Sources* **2019**, *412*, 204–223. [CrossRef]
52. Isaac, J.A.; Mangani, L.R.; Devaux, D.; Bouchet, R. Electrochemical Impedance Spectroscopy of PEO-LATP Model Multilayers: Ionic Charge Transport and Transfer. *ACS Appl. Mater. Interfaces* **2022**, *14*, 13158–13168. [CrossRef] [PubMed]
53. Hovington, P.; Lagacé, M.; Guerfi, A.; Bouchard, P.; Mauger, A.; Julien, C.M.; Armand, M.; Zaghib, K. New lithium metal polymer solid state battery for an ultrahigh energy: Nano C-$LiFePO_4$ versus nano $Li_{1.2}V_3O_8$. *Nano Lett.* **2015**, *15*, 2671–2678. [CrossRef] [PubMed]
54. Chen, R.J.; Zhang, Y.B.; Liu, T.; Xu, B.Q.; Lin, Y.H.; Nan, C.W.; Shen, Y. Addressing the Interface Issues in All-Solid-State Bulk-Type Lithium Ion Battery via an All-Composite Approach. *ACS Appl. Mater. Interfaces* **2017**, *9*, 9654–9661. [CrossRef] [PubMed]
55. Park, M.S.; Jung, Y.C.; Kim, D.W. Hybrid solid electrolytes composed of poly(1,4-butylene adipate) and lithium aluminum germanium phosphate for all-solid-state Li/$LiNi_{0.6}Co_{0.2}Mn_{0.2}O_2$ cells. *Solid State Ion.* **2018**, *315*, 65–70. [CrossRef]
56. Ates, T.; Keller, M.; Kulisch, J.; Adermann, T.; Passerini, S. Development of an all-solid-state lithium battery by slurry-coating procedures using a sulfidic electrolyte. *Energy Storage Mater.* **2019**, *17*, 204–210. [CrossRef]

57. Porcarelli, L.; Aboudzadeh, M.A.; Rubatat, L.; Nair, J.R.; Shaplov, A.S.; Gerbaldi, C.; Mecerreyes, D. Single-ion triblock copolymer electrolytes based on poly(ethylene oxide) and methacrylic sulfonamide blocks for lithium metal batteries. *J. Power Sources* **2017**, *364*, 191–199. [CrossRef]
58. Bouchet, R.; Maria, S.; Meziane, R.; Aboulaich, A.; Lienafa, L.; Bonnet, J.P.; Phan, T.N.T.; Bertin, D.; Gigmes, D.; Devaux, D.; et al. Single-ion BAB triblock copolymers as highly efficient electrolytes for lithium-metal batteries. *Nat. Mater.* **2013**, *12*, 452–457. [CrossRef]
59. Wakayama, H.; Yonekura, H.; Kawai, Y. Three-Dimensional Bicontinuous Nanocomposite from a Self-Assembled Block Copolymer for a High-Capacity All-Solid-State Lithium Battery Cathode. *Chem. Mater.* **2016**, *28*, 4453–4459. [CrossRef]
60. Noh, H.J.; Youn, S.; Yoon, C.S.; Sun, Y.K. Comparison of the structural and electrochemical properties of layered $Li[Ni_xCo_yMn_z]O_2$ (x=1/3, 0.5, 0.6, 0.7, 0.8 and 0.85) cathode material for lithium-ion batteries. *J. Power Sources* **2013**, *233*, 121–130. [CrossRef]
61. Krauskopf, T.; Hartmann, H.; Zeier, W.G.; Janek, J. Toward a Fundamental Understanding of the Lithium Metal Anode in Solid-State Batteries-An Electrochemo-Mechanical Study on the Garnet-Type Solid Electrolyte $Li_{6.25}Al_{0.25}La_3Zr_2O_{12}$. *ACS Appl. Mater. Interfaces* **2019**, *11*, 14463–14477. [CrossRef]
62. Wu, S.L.; Javier, A.E.; Devaux, D.; Balsara, N.P.; Srinivasan, V. Discharge Characteristics of Lithium Battery Electrodes with a Semiconducting Polymer Studied by Continuum Modeling and Experiment. *J. Electrochem. Soc.* **2014**, *161*, A1836–A1843. [CrossRef]